LHC dark matter signals from vector resonances and top partners

Alexander S. Belyaev,[1,2] Thomas Flacke,[3] Bithika Jain,[4,5] and Patrick B. Schaefers[1]

[1]*School of Physics & Astronomy, University of Southampton, Southampton SO17 1BJ, United Kingdom*
[2]*Particle Physics Department, Rutherford Appleton Laboratory, Chilton, Didcot, Oxon OX11 0QX, United Kingdom*
[3]*Center for Theoretical Physics of the Universe, Institute for Basic Science (IBS), Daejeon 34126, Korea*
[4]*ICTP South American Institute for Fundamental Research & Instituto de Física Teórica Universidade Estadual Paulista, 01140-070 São Paulo, Brazil*
[5]*School of Physics, Korea Institute for Advanced Study, Seoul 02455, Korea*

(Received 14 February 2018; published 15 August 2018)

Extensions of the standard model which address the hierarchy problem and dark matter (DM) often contain top partners and additional resonances at the TeV scale. We explore the phenomenology of a simplified effective model with a vector resonance Z', a fermionic vectorlike colored partner of the top quark T' as well as a scalar DM candidate ϕ and provide publicly available implementations in `CalcHEP` and `MadGraph`. We study the $pp \to Z' \to T'\overline{T'} \to t\bar{t}\phi\phi$ process at the LHC and find that it plays an important role in addition to the $T'\overline{T'}$ production via strong interactions. It turns out that the presence of the Z' can provide a dominant contribution to the $t\bar{t} + \not{E}_T$ signature without conflicting with existing bounds from Z' searches in di-jet and di-lepton final states. We find that, through this process, the LHC is already probing DM masses up to about 900 GeV and top partner masses up to about 1.5 TeV, thus exceeding the current bounds from QCD production alone almost by a factor of 2 for both particles.

DOI: 10.1103/PhysRevD.98.035019

I. INTRODUCTION

The Higgs boson discovery in July 2012 [1,2] was a remarkable celebration of the unprecedented success of the standard model (SM), which was missing this last particle. At the same time, this announcement has opened a new chapter in the exploration of physics beyond the standard model (BSM). BSM physics is necessary to solve the principal problems of the SM among which are (a) the naturalness/fine-tuning problem on theory side and the related hierarchy between the Higgs mass and the Planck scale; (b) the dark matter (DM) problem on the experimental side at the cosmological scale—the SM does not provide any viable DM candidate, while the existence of DM has been established beyond any reasonable doubt. There are several appealing classes of theories which have the potential to solve these problems, and in these theories, the properties of the Higgs boson (either as a composite state or a fundamental particle) are compatible with those of the 125 GeV scalar discovered at the LHC.

Among these theories is supersymmetry (SUSY) [3–6], which solves the hierarchy problem in the fundamental Higgs sector via fermion-boson symmetry and provides dark matter candidates. A very attractive alternative to SUSY is technicolor (TC) [7,8], in which the electroweak (EW) symmetry is broken by strong dynamics in analogy to QCD. In these models, the Higgs boson is the bound state of new fundamental particles involved in these new strong dynamics, however in spite of the qualitatively different nature, the Higgs properties can be similar to those of the SM Higgs and consistent with the LHC data [9]. Another set of promising BSM theories are composite Higgs (CH) scenarios [10–12] (see also recent developments starting from [13]), in which the new gauge dynamics do not break the electroweak symmetry, but spontaneously break a global symmetry of the high energy model [14]. Lastly, both TC and CH models always predict integer spin bound states, which we incorporate minimally in our model in form of a Z' boson to account for this theory prediction. Further alternatives include Randall-Sundrum models [16,17], little Higgs models [18–20], as well as twin-Higgs models [21] also known as neutral naturalness [22].

Many of the nonsupersymmetric models mentioned above include a top partner sector which often plays an important role in keeping the models technically natural. Especially for TC and CH models, the top partners are bound states of the new strong dynamics and provide an

elegant alternative to SUSY to solve the hierarchy problem. Furthermore, the models typically contain the above mentioned BSM resonances at the TeV scale, and—if they (or their extensions) also address DM—a parity (or a larger symmetry group) keeping dark matter stable as well as a parity-odd dark matter sector.

In this article, we explore the phenomenology of a simplified model, which incorporates these ingredients at the level of an effective theory with a vector resonance Z' as a consequence of the TC and CH predictions of integer spin bound states, a fermionic vectorlike colored partner of the top quark T' as well as a scalar dark matter candidate ϕ arising via minimal gauge-invariant Yukawa interactions $\lambda_{\phi T' t}$. As a consequence of this coupling and the desired DM stability, both ϕ and the top partners have the same parity (which we assume to be negative DM parity). In particular, we study the process $pp \to Z' \to T'\overline{T'} \to t\bar{t}\phi\phi$, in which the $T'\overline{T'}$ pair coming from the Z' decay gives rise to a $t\bar{t}+$ missing transverse momentum signature, $t\bar{t}+\not{E}_T$. The $t\bar{t}+\not{E}_T$ signature from the Z' resonance has not been studied previously and, as we show, its new topology has different kinematical distributions in comparison to the $t\bar{t}+\not{E}_T$ signature coming from QCD production of $T'\overline{T'}$, which has been studied in [23–25]. Besides introducing kinematics different from QCD $T'\overline{T'}$-pair production, the presence of the Z' can also provide an additional, potentially even dominant contribution to the pair production rate of top partners without conflicting with existing bounds from Z' searches in di-jet and di-lepton final states. A similar observation has been made before in the context of pair production enhancement of charge $5/3$ top partners through $SU(2)$ triplet vector resonances [26]. As we will show, the Z', T' and DM masses can be probed with the $t\bar{t}+\not{E}_T$ signature well beyond the reach coming only from QCD production.

This article is organized as follows: In Sec. II, we present the model and discuss its parameter space. In Sec. III, we describe the analysis setup, present a parton-level analysis, study gluon-Z' interference effects, explore the model constraints from di-jet and di-lepton LHC searches and eventually present the LHC potential to explore the model parameter space including the masses $M_{Z'}$, $M_{T'}$ and $m_{\rm DM} \equiv m_\phi$ with the $t\bar{t}+\not{E}_T$ signature. Lastly, we draw our conclusions in Sec. IV.

II. A SIMPLIFIED MODEL WITH VECTOR RESONANCES, TOP PARTNERS AND SCALAR DM

A. The model

As outlined in the Introduction, many models like composite Higgs models or models with extra dimensions contain top partners as well as vector resonances as part of their TeV scale particle spectrum, and a dark matter candidate (whose stability is protected by a discrete symmetry) is desirable in order to explain the observed dark matter relic density.

For our study, we use a simplified effective model which contains these ingredients in order to study the implications of their interplay for LHC searches. We consider a Z' model where the Z' vector resonance couples to SM quarks and leptons and to top partners T'_s (SU(2) singlet) or $Q' = (T'_d, B'_d)$ (SU(2) doublet) [27]. We also include a neutral scalar ϕ. The top partners and ϕ are assumed to carry negative DM parity with $m_{T'} > m_\phi$, while SM particles and the Z' carry positive DM parity. This makes ϕ a stable DM candidate, which couples to both top quarks and top partners. The only other renormalizable DM couplings comprise a Higgs-portal coupling term $HH^\dagger\phi^2$ and DM self-interactions ϕ^4. The detailed Langrangian for the model, which we abbreviate as ZP-TP-DM model reads

$$\mathcal{L} = \mathcal{L}_{\rm SM} + \mathcal{L}_{\rm kin} + \mathcal{L}_{Z'q} + \mathcal{L}_{Z'\ell} + \mathcal{L}_{Z'Q'} + \mathcal{L}_{\phi Q'} - V_\phi \quad (1a)$$

$$\mathcal{L}_{\rm kin} = -\frac{1}{4}(\partial_\mu Z'_\nu - \partial_\nu Z'_\mu)(\partial^\mu Z'^\nu - \partial_\nu Z'^\mu) + \frac{M^2_{Z'}}{2} Z'_\mu Z'^\mu + \frac{1}{2}\partial_\mu\phi\partial^\mu\phi - \frac{m^2_\phi}{2}\phi^2 + \overline{T'_s}(i\not{D} - M_{T'_s})T'_s + \overline{Q'_d}(i\not{D} - M_{T'_d})Q'_d, \quad (1b)$$

$$\mathcal{L}_{Z'q} = \lambda_{Z'q\bar{q},L/R} Z'_\mu (\bar{q}_{L/R}\gamma^\mu q_{L/R}), \quad (1c)$$

$$\mathcal{L}_{Z'\ell} = \lambda_{Z'\ell^+\ell^-,L/R} Z'_\mu (\bar{\ell}_{L/R}\gamma^\mu \ell_{L/R}), \quad (1d)$$

$$\mathcal{L}_{Z'Q'} = \lambda_{Z'T'_s\overline{T'_s},L/R} Z'_\mu (\overline{T'_{s,L/R}}\gamma^\mu q_{L/R}) + \lambda_{Z'T'_d\overline{T'_d},L/R} Z'_\mu (\overline{T'_{d,L/R}}\gamma^\mu T'_{d,L/R}) + \lambda_{Z'T'_d\overline{T'_d},L/R} Z'_\mu (\overline{B'_{d,L/R}}\gamma^\mu B'_{d,L/R}), \quad (1e)$$

$$\mathcal{L}_{\phi Q'} = (\lambda_{\phi T'_s t}\phi\bar{t}_R T'_{s,R} + \lambda_{\phi T'_d t}\phi\bar{t}_L T'_{d,L} + \lambda_{\phi T'_d t}\phi\bar{b}_L B'_{d,L}) + \text{H.c.}, \quad (1f)$$

$$V_\phi = \frac{\lambda_\phi}{4!}\phi^4 + \frac{\lambda_{\phi H}}{2}\phi^2\left(|H|^2 - \frac{v^2}{2}\right). \quad (1g)$$

In general, the Z' is not necessarily associated to a gauge symmetry and the couplings are "current couplings" (and thus not restricted by gauge invariance). We, therefore, leave the couplings of the Z' to SM quarks, leptons, and top partners as free parameters. We write the DM interaction with the Higgs doublet such that the electroweak contribution to the mass of ϕ is absorbed, and m_ϕ is the physical mass of ϕ. One should note that DM-Higgs interactions do not affect the LHC $t\bar{t}+\not{E}_T$ signature under study. However, these interactions are important for the constraints on the model parameter space from relic density, DM direct (DD) and indirect (ID) detection experiments, as well as for $h \to \phi\phi$ invisible Higgs boson decay limits at the LHC.

In spite of the many parameters appearing even in the simplified model given by Eq. (1), the number of parameters which are relevant to the $t\bar{t}+\not{E}_T$ signature under study at the LHC, DM searches in DD and ID experiments as well as Higgs physics at the LHC is much more reduced as we discuss in the following section.

B. The model parameter space and analysis setup

We are studying the $t\bar{t}+\not{E}_T$ final state in this article, which receives contributions from T'-pair production either through QCD interactions or through resonant Z' production with $Z' \to T'\overline{T'}$. For the $t\bar{t}+\not{E}_T$ signature at the LHC coming from the QCD $T'\overline{T'}$-pair production, the only relevant parameters are $M_{T'}$ and m_ϕ. In this work, we perform a detailed study of singlet T' (T'_s) pair production. Doublet T' (T'_d) pair production is expected to have very similar phenomenology [29].

The Z' contribution to the signature under study adds $M_{Z'}$ and the Z' couplings to SM quarks and leptons as well as Z' couplings to T'_s to the parameter space. In Sec. III, we demonstrate that the differences between the four possible chiral coupling combinations for $\lambda_{Z'q\bar{q},L/R}$ and $\lambda_{Z'T'_s\overline{T}'_s,L/R}$ (i.e., LL, RR, LR, RL) are negligible when studying the $t\bar{t}+\not{E}_T$ signature. Therefore, it is sufficient to consider just one coupling combination and we choose it to be LL, i.e., the case where $\lambda_{Z'q\bar{q},L}$ and $\lambda_{Z'T'_s\overline{T}'_s,L}$ are nonzero and all right-handed couplings vanish. We also consider the case of a nonvanishing Z' coupling to SM leptons and choose $\lambda_{Z'\ell^+\ell^-,L} = \lambda_{Z'q\bar{q},L}$, from which results for other coupling ratios can be inferred.

The complete set of model parameters relevant to our study of the $t\bar{t}+\not{E}_T$ signature at the LHC comprises five parameters:

$$M_{T'_s}, \qquad m_\phi, \qquad M_{Z'}, \qquad \lambda_{Z'q\bar{q},L}, \qquad \lambda_{Z'T'_s\overline{T}'_s,L}. \tag{2}$$

The DM phenomenology—in particular the DM relic density as well as DM direct and indirect detection—depends on two more parameters,

$$\lambda_{\phi H} \quad \text{and} \quad \lambda_{\phi T'_s t}, \tag{3}$$

whose effects in combination with the top partners and Z' boson within this new model are illustrated below. Before doing so, we describe our analysis setup to gather the results on the DM relic density as well as direct and indirect detection limits in the remainder of this section. The analysis setup used to perform the collider analysis is described in the next section.

We have implemented the model described by the Lagrangian in Eq. (1) using the `LanHEP` [31–33] and `FeynRules` [34,35] packages for `CalcHEP` [36] and `MadGraph5_aMC@NLO` [37], respectively. The implementations have been cross-checked against each other for scattering and decay processes and are available at HEPMDB [38] under hepmdb:0717.0253 [39] (`CalcHEP`) and hepmdb:0717.0254 [40] (`Madgraph`), where—among other features—events can be generated online right away using the web page interface. For the parton level studies and simulations, we use `MadGraph5_aMCNLO 2.3.3` and `CalcHEP 3.6.27` with the `NNPDF2.3QED` PDF [41]. For both QCD renormalization and PDF factorization scales, we used $Q = M_{Z'}$. In our study, we do not apply NLO k-factors to the signal, so our results on the exclusion of the parameter space are conservative.

Hadronization and parton showering were performed via `Pythia v8.219` [42] with subsequent fast detector simulation performed using `Delphes 3` [43] and `FastJet v.3.1.3` [44,45] with a cone radius $\Delta R = 0.4$ for the jet reconstruction. The detector level analysis was performed using `CheckMATE 2.0.0` [46,47] to probe the $t\bar{t}+\not{E}_T$ signature against the current $\sqrt{s} = 13$ TeV ATLAS and CMS constraints [48–59].

For illustration purposes and in order to stress the complementarity of collider and noncollider searches, we have evaluated the DM relic density $\Omega_{\rm DM}h^2$ with the latest version of the `micrOMEGAs v4.3.5` package [60–62], which directly reads the model files in `CalcHEP` format. We have also checked the model parameter space for consistency with the limits from DM direct detection (DD) experiments. To do so, we have evaluated the spin-independent cross section of DM scattering off the proton σ_{SI} for the first time at one-loop level using the `micrOMEGAs` package and compared it to the latest and so far strongest DM DD limit from the Xenon 1 Ton experiment [63]. Since digital data were not provided in the above paper, we have digitized the limit and uploaded it to the PhenoData database [64]. One should also note that the latest version of `micrOMEGAs` mentioned above correctly evaluates the one-loop-induced DM scattering rates on nuclei exactly since this loop was implemented by hand as a library for the respective loop diagrams.

In Fig. 1, we present LHC, DM Direct Detection (DD) and relic density constraints on the parameter space of the ZP-TP-DM model in the $(\frac{M_{T'_s}}{m_\phi}, m_\phi)$ plane for $\lambda_{\phi H} = 0$, i.e., for the case in which the relic density is fully determined by co-annihilation of ϕ with the T', without any contribution from ϕ interactions with the Higgs.

The green-shaded area indicates the current LHC exclusion region for the $t\bar{t}+\not{E}_T$ signature coming from $pp \to T'\overline{T'} \to t\bar{t}\phi\phi$, mediated by gluon exchange only (no Z' exchange). These bounds will be discussed in detail in Sec. III D. The thin dashed lines with the respective labels indicate the iso-levels of $M_{T'_s}$ in GeV. The exclusion area qualitatively agrees with the one found in [25], however its lower edge corresponding to lower $M_{T'_s}$ is slightly extended in our study, since in addition to `ATLAS_CONF_2016_050` [58] we are using results of

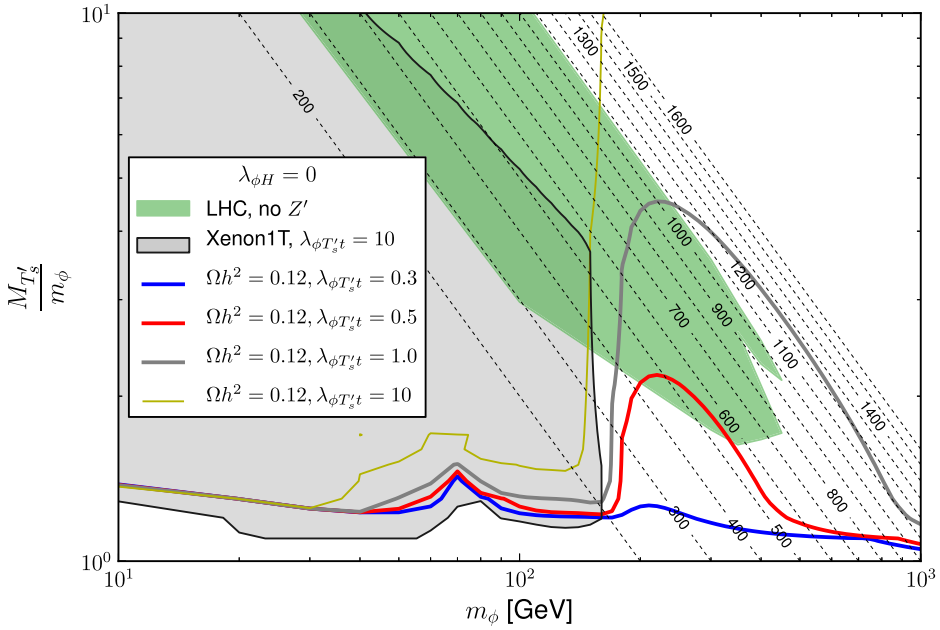

FIG. 1. LHC, DM Direct Detection and relic density constraints on the parameter space of the ZP-TP-DM model in the $\left(\frac{M_{T'_s}}{m_\phi}, m_\phi\right)$ plane for $\lambda_{\phi H} = 0$. The green-shaded area indicates the current LHC exclusion region for the $t\bar{t} + \not{E}_T$ signature coming from the process $pp \to T'\overline{T'} \to t\bar{t}\phi\bar{\phi}$ mediated only by gluon exchange (no Z' exchange). The grey-shaded area indicates the exclusion region from DM direct detection from the latest Xenon 1 Ton data [63] for $\lambda_{\phi T'_s t} = 10$. The parameter space above the blue, red, grey and yellow contours is excluded by the relic density constraints for $\lambda_{\phi T'_s t} = 0.3$, 0.5, 1, and 10, respectively, with each contour corresponding to the $\Omega h^2 = 0.12$ iso-level. The thin dashed lines with the respective labels indicate the iso-levels of $M_{T'_s}$ in GeV.

ATLAS_1604_07773 [50], which are more sensitive to a smaller mass gap between DM and the T'_s. Figure 1 also holds the exclusion region from DM direct detection based on the latest Xenon 1 Ton data [63] for $\lambda_{\phi T'_s t} = 10$, shown as grey-shaded area. One should note that for smaller values of $\lambda_{\phi T'_s t} = 0.3$, 0.5, and 1.0, which are chosen as other benchmarks for this plot, Xenon 1 Ton does not have any sensitivity to the parameter space yet, since the cross section for DM scattering off nuclei scales quadratically with $\lambda_{\phi T'_s t}$, limiting the experiment to probe only large values of $\lambda_{\phi T'_s t}$ at the moment.

Also, in Fig. 1, the blue, red, grey, and yellow contours (for $\lambda_{\phi T'_s t} = 0.3$, 0.5, 1, and 10, respectively) show the parameter values which reproduce a relic density of $\Omega h^2 = 0.12$, corresponding to the value observed by PLANCK [65,66]. The parameter space above these lines (for the respective value of $\lambda_{\phi T'_s t}$) yields too large relic densities and is thus excluded. From Fig. 1, one can see that the LHC plays an important and complementary role to DM DD and relic density constraints in covering the $m_\phi > m_t$ region, which is not fully constrained by noncollider experiments, especially for not-so-small values of $\lambda_{\phi T'_s t}$. One should also note that the allowed parameter space in the $(\frac{M_{T'_s}}{m_\phi}, m_\phi)$ plane can be affected by nonzero $\lambda_{\phi H}$. The relic abundance can be strongly altered in this case, because DM can annihilate through Higgs interactions instead of co-annihilation with the top partner. At the same time, direct detection bounds are modified as the DM can now interact with nuclei via Higgs exchange. Finally, the Higgs can decay into DM if the DM is sufficiently light, which yields additional bounds from LHC Higgs measurements. In Fig. 2, we show the resulting bounds for fixed $\lambda_{\phi T'_s t} = 1$ and two cases of $\lambda_{\phi H} = 0.1$ (left) and 0.3 (right). One can see that also for nonzero $\lambda_{\phi T'_s t}$, the very narrow region for m_ϕ around $M_H/2$ is allowed by noncollider searches, because in this region, the relic density is strongly reduced due to resonant DM annihilation into a Higgs boson, while DM DD rates, which are rescaled with the relic density, are also suppressed. At the same time, this region can be effectively probed by the LHC. As an illustration, the pink-shaded area indicates the limit from the invisible Higgs decay searches from ATLAS [67], which exclude $\mathrm{BR}(H \to \text{invisible}) < 28\%$ at 95% CL. Eventually, this limit is relevant for $m_\phi < M_H/2$ and sufficiently large ($\simeq$0.015) values of $\lambda_{\phi H}$.

As mentioned above, we present the noncollider constraints for illustration purposes only. Since the Z' does not affect the noncollider DM phenomenology for this model, we refer the reader to Refs. [25,30] for a detailed exploration of the DM direct and indirect collider constraints, where an analogous model, but without the Z', was studied. We also refer the reader to other works on scalar singlet DM (see e.g., Ref. [68] and the references therein), which are relevant for the case when heavy top partners are decoupled.

Finally, we would like to note that there is a special region of the parameter space, where the mass gap between

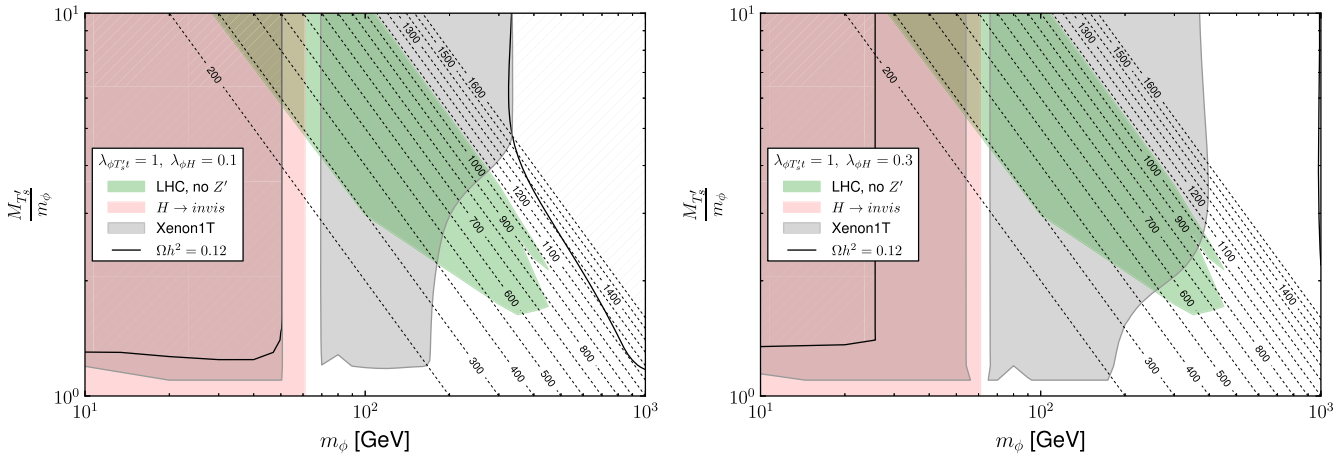

FIG. 2. LHC, DM Direct Detection and relic density constraints on the parameter space of the ZP-TP-DM model in the $\left(\frac{M_{T'_s}}{m_\phi}, m_\phi\right)$ plane for $\lambda_{\phi T'_s t} = 1$ and two values of $\lambda_{\phi H} = 0.1$ (left) and 0.3 (right): (a) the green-shaded area indicates the current LHC exclusion region from the process $pp \to T'\bar{T}' \to t\bar{t}\phi\bar{\phi}$ without Z' exchange; (b) the grey-shaded area indicates the exclusion region from DM DD from the latest Xenon 1 Ton data [63]; (c) the hatched parameter space is excluded by relic density constraints; (d) the pink-shaded area indicates the limit from the invisible Higgs decay searches. The thin dashed lines indicate the iso-levels of $M_{T'_s}$ in GeV.

m_ϕ and $M_{T'_s}$ is small. In this region, where the relic density is equal or below the PLANCK constraint, the T'_s decays to DM, soft b-jets and light jets or leptons (coming from virtual top quark decays). This case is very similar to the case of SUSY with degenerate stops and neutralinos and requires a dedicated analysis beyond the scope of this work, where we focus on the role of the Z' boson to extend the LHC reach of the ZP-TP-DM parameter space for the case where $M_{T'_s} - m_\phi > m_t$.

III. ANALYSIS OF $pp \to Z' \to T'_s\overline{T'_s} \to t\bar{t}\phi\phi$ FOR THE LHC

In this study, we focus on Z' production, where the Z' then decays to a T'_s-pair which further decays into the final state consisting of two top quarks and DM, i.e., $t\bar{t}\phi\phi$. The same final state also arises from QCD pair production of $T'_s\overline{T'_s}$. The corresponding Feynman diagrams are shown in Fig. 3.

We start our investigation with several pre-studies and checks. In Sec. III A, we investigate the dependence of kinematic distributions on the chirality of the couplings involved in the Z' production and its subsequent cascade-decay. We will find that the chirality of the couplings $\lambda_{Z'q\bar{q}}$, $\lambda_{Z'T'_s\overline{T'_s}}$ and $\lambda_{\phi' T'_s \bar{t}}$ have a minor influence on the kinematics at parton level. This justifies to pick one specific set of chiralities for further studies, which we choose as $\lambda_{Z'q\bar{q},L}$ and $\lambda_{Z'T'_s\overline{T'_s},L}$, and we consider an $SU(2)$ singlet top partner (implying a coupling to ϕ and t_R). Similar minor differences in the kinematics can also be expected in the T'_d case.

As two further prestudies, in Sec. III B, we explicitly check that interference between the Z' produced and QCD produced $T'_s\overline{T'_s}$-pair is very small and not relevant to our studies, while in Sec. III C we quantify finite-Z'-width effects.

To determine the constraints from LHC searches on the model parameter space, we first determine the constraints on QCD-only $T'\overline{T'_s}$-pair production in Sec. III D. The details of the LHC searches used are specified at the end of that subsection. In Sec. III E, we determine the bounds on the couplings $\lambda_{Z'q\bar{q}}$ and $\lambda_{Z'T'_s\overline{T'_s}}$ from di-lepton and di-jet resonance searches, which arise due to the Z' being allowed to also decay into $q\bar{q}$ and $\ell^+\ell^-$. In Sec. III F, we determine the improved bounds on the $(\lambda_{Z'q\bar{q}}, \lambda_{Z'T'_s\overline{T'_s}})$ parameter space when LHC SUSY search bounds are applied for the process $pp \to Z' \to T'_s\overline{T'_s} \to t\bar{t}\phi\phi$. Section III G contains a detailed benchmark analysis.

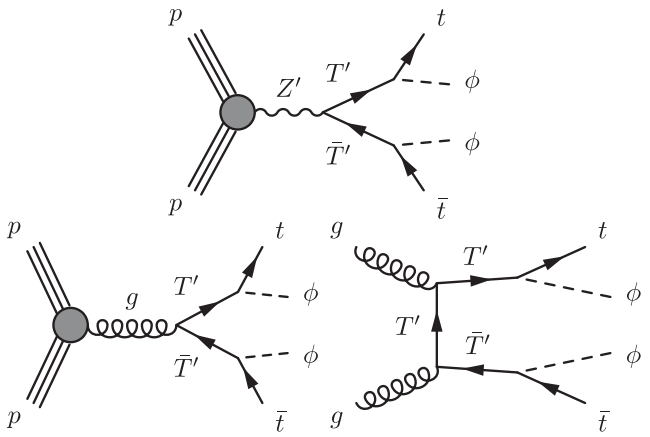

FIG. 3. Feynman diagrams for $t\bar{t}\phi\phi$ production via T'_s decays from Z' bosons (top) and gluons (bottom).

A. Prestudy I: Impact of chiral couplings on kinematical distributions

In order to understand the parameter space and the effect from different Z' coupling combinations on the kinematical properties of the signature under study, we explore several parton level distributions shown in Figs. 4 and 5. These distributions have been obtained using the `MadGraph5_aMCNLO 2.3.3` framework in conjunction with `MadAnalysis`. We present results for the four different chiral combinations: "LL", "LR", "RL", "RR", where the first letter indicates the chirality of $\lambda_{Z'q\bar{q}}$ and the second letter indicates the chirality of $\lambda_{Z'T_s'\overline{T_s'}}$. The couplings themselves are fixed to $\lambda_{Z'q\bar{q}} = 0.25$ and $\lambda_{Z'T_s'\overline{T_s'}} = 2.5$, while the different masses are set to $M_{Z'} = 3$ TeV, $M_{T_s'} = 1$ TeV and $m_\phi = 500$ GeV. All events are generated for the process where T_s' are pair-produced via Z' bosons only. From Fig. 4 (top panel), one can see that the $\not{E}_T$ spectrum (evaluated from DM momentum only) and the invariant mass distributions of the di-tops barely depend on the choice of a chiral combination. Minor deviations only occur in the high energy tails. In Sec. III G below, we show that the difference between the cut-flow efficiencies for the two extreme cases "LL" and "RR" is at the level of 1%–2%, which quantitatively proves our point to choose just one chiral combination and significantly reduce the model parameter space.

The pseudorapidity (η) distributions of the top and antitop quark are very similar for the LL and LR chiral combinations [69]. Likewise, the top/antitop pseudorapidity distributions (Fig. 4, bottom left) for the RL and RR combination are close to each other, but slightly wider

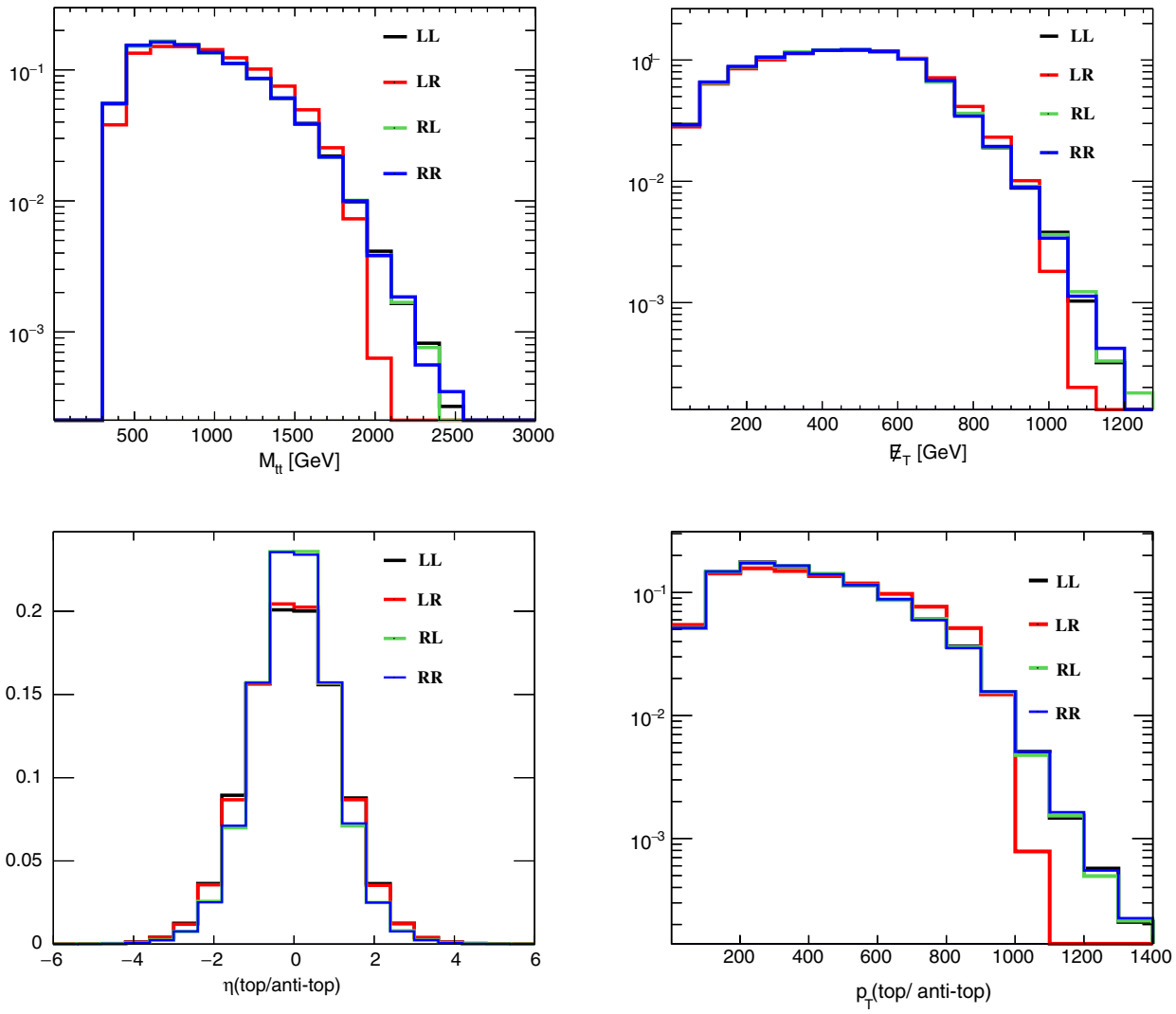

FIG. 4. Differential distributions (normalized to one) for different chiral choices of $\lambda_{Z'q\bar{q},L/R}$ (first letter) and $\lambda_{Z'T_s'\overline{T_s'},L/R}$ (second letter), when top partner production only via Z' bosons is considered. The produced top partners decay to top quarks and dark matter. LL is shown in black, LR in red, RL in green, and RR in blue. The BSM particle masses are chosen as $M_{Z'} = 3$ TeV, $M_{T_s'} = 1$ TeV and $m_\phi = 500$ GeV.

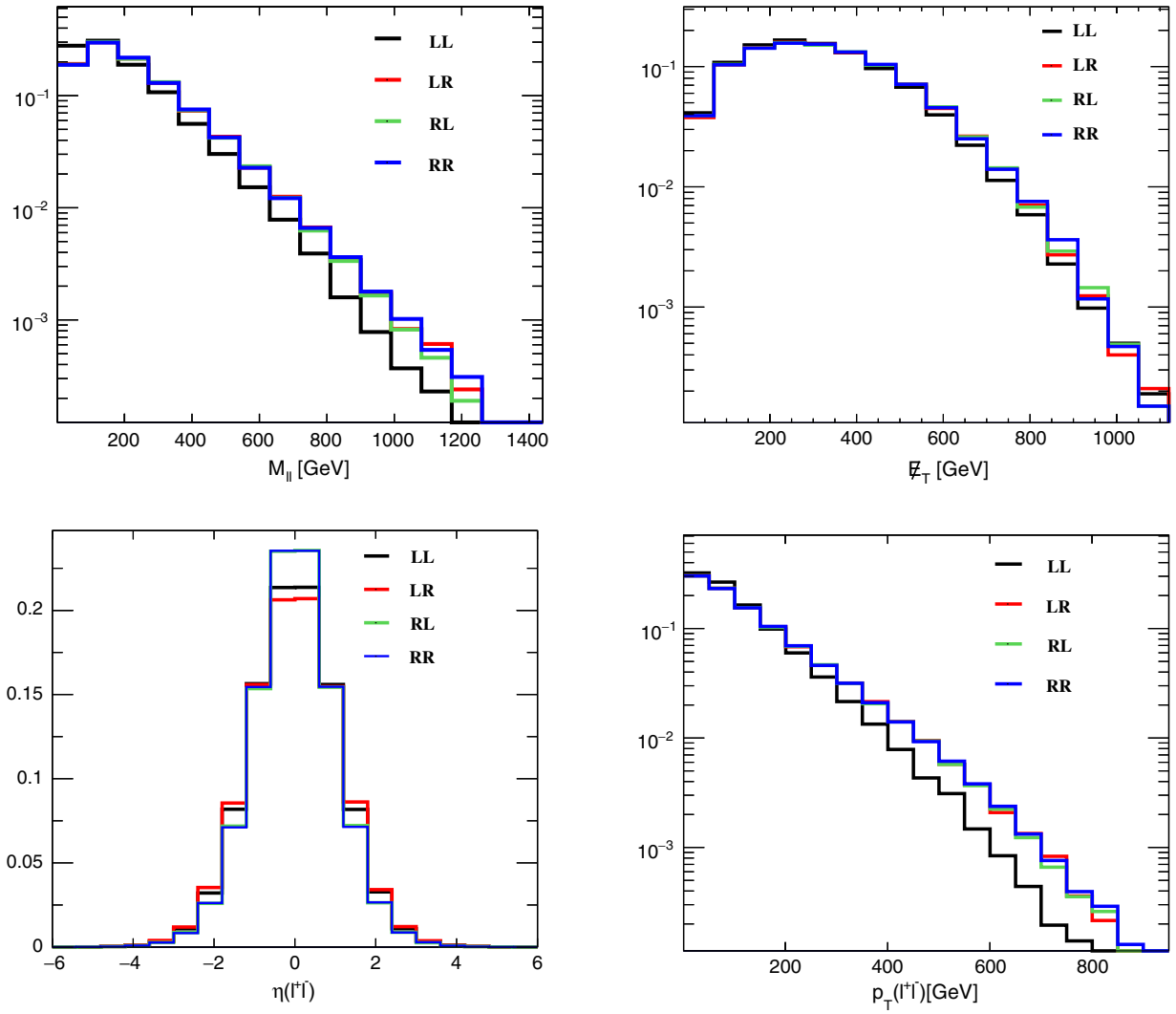

FIG. 5. Differential distributions (normalized to one) for different chiral choices of $\lambda_{Z'q\bar{q},L/R}$ (first letter) and $\lambda_{Z'T_s'\overline{T_s'},L/R}$ (second letter) when top partner production only via Z' bosons is considered. The produced top partners decay to tops and dark matter, with the top quarks decaying further into bW_{lep}. LL is shown in black, LR in red, RL in green, and RR in blue. The BSM particle masses are chosen as $M_{Z'} = 3$ TeV, $M_{T_s'} = 1$ TeV and $m_\phi = 500$ GeV.

compared to the LL and LR distributions. The transverse momentum for top and antitop quarks changes marginally in the high p_T tail (for $p_T \gtrsim 1$ TeV), when the chirality of $\lambda_{Z'q\bar{q}}$ changes.

The above (not directly observable) distributions define kinematics of the top quark decay products, which we present next in Fig. 5. For a leptonic W decay, one can see that the RR and LR combinations have the same p_T distributions of the leptons. The same is true for the LL and RL combinations. For RR and LR, however, this distribution has a slightly higher tail (slightly harder) in comparison to LL and RL. This behavior has been observed previously (see Ref. [24]) and occurs due to the influence of the top polarization on the p_T of the decay products. This difference in lepton p_T distributions occurs for high values of the lepton p_T and does not visibly affect the efficiency of the cuts for the signature under study. The same holds for the $M_{\ell\ell}$, η_ℓ and $\not{E}_T$ distributions. One can note the slight difference in η_ℓ is correlated with the slight difference in η_t for different chiral combinations. Also, the $\not{E}_T$ shape before and after a top quark decays are very similar. For simplicity, we work with the case where both $\lambda_{Z'q\bar{q}}$ and $\lambda_{Z'T_s'\overline{T_s'}}$ are left-handed (LL). This choice yields a (marginally) softer lepton p_T and, therefore, slightly lower cut-efficiencies compared to LR and RR, making the LL configuration a conservative choice.

It is also instructive to explore the difference in kinematics between the setup where top partners are produced via gluons and for the combined production involving both Z' bosons and gluon mediation. This difference is directly related to the main point of our paper—the role of the Z' boson in exploring the $t\bar{t} + \not{E}_T$ signature at the LHC.

In Fig. 6, we present kinematical distributions for two points with $M_{Z'} = 2.5$ TeV and 3 TeV with $\lambda_{Z'q\bar{q}}$ and $\lambda_{Z'T_s'\overline{T_s'}}$ taken to be left-handed and kept at $\lambda_{Z'q\bar{q}} = 0.25$ and $\lambda_{Z'T_s'\overline{T_s'}} = 2.5$. One can see that the lepton p_T distributions are similar for gluon exchange alone and $g + Z'$ exchange for both Z' masses. However, one can also observe that the transverse momentum of the ℓ^+ as well as $\not{E}_T$ are systematically harder in the $g + Z'$ exchange case, especially for larger p_T or $\not{E}_T$. As we will see later from the fast detector simulation studies, these differences lead to a non-negligible difference of the final selection efficiencies, which are higher for $g + Z'$ exchange in comparison to just gluon exchange alone.

B. Prestudy II: Interference effects

Besides T_s'-pair production via Z' bosons, T_s'-pairs are also produced through QCD interactions, as shown in Fig. 3. To quantify possible interference effects, we study the three cases where T_s'-pairs are produced only via Z' bosons, only via gluons, and for the combined production involving both Z' bosons and gluons using `MadGraph5 2.3.3`. Additionally, we try to maximize the interference effects by choosing the couplings and masses such that the Z'-mediated and gluon-only cross sections are nearly identical. Because the Z' width can also affect interference, we study two parameter points: one with a narrow Z' width ($M_{Z'} = 2.5$ TeV, $M_{T_s'} = 1$ TeV, $\lambda_{Z'q\bar{q}} = 0.3$, $\lambda_{Z'T_s'\overline{T_s'}} = 0.58$) and one with a very broad Z' width ($M_{Z'} = 2.5$ TeV, $M_{T_s'} = 1$ TeV, $\lambda_{Z'q\bar{q}} = 0.21$, $\lambda_{Z'T_s'\overline{T_s'}} = 4.7$). The results are summarized in Table I.

We find the interference to be constructive and ranging from +2.5% gain in cross section in the narrow-width scenario to +3.6% in the broad width scenario.

C. Prestudy III: Narrow-width approximation and corrections

The narrow-width approximation (NWA) enables us to easily estimate and scale cross sections for variable model parameters, such as couplings and masses. However, as the NWA becomes less accurate with an increasing width of the decaying particle, it is important to study and estimate corrections to it. In Fig. 7, we show the cross sections for $pp \to Z' \to T_s'\overline{T_s'}$ [70] in the NWA (black line) and computed with `CalcHEP` (red '+') for $M_{Z'} = 3$ TeV, $M_{T_s'} = 1.2$ TeV, $\lambda_{Z'q\bar{q}} = 0.1$, $\lambda_{Z'\ell^+\ell^-} = 0$ and varying $\lambda_{Z'T_s'\overline{T_s'}}$. The relative difference between the two (normalized to the `CalcHEP` result) is shown as blue crosses. For very small $\Gamma_{Z'}/M_{Z'}$ up to approximately 1%, the NWA perfectly estimates the cross section without any approximation σ. Increasing $\Gamma_{Z'}/M_{Z'}$ to ≈5% yields a difference in cross section of roughly 10%. Further increasing $\Gamma_{Z'}/M_{Z'}$ leads to relative differences of 40% or more, therefore making the NWA very inaccurate in that region. Also note that the NWA for this particular choice of $M_{Z'}$ and $M_{T_s'}$ always overestimates the actual cross section, which would lead to over-optimistic limits and constraints. To correct for finite width effects, we use our simulation results in Fig. 7 to define a correction factor $\kappa(\lambda^2_{Z'T_s'\overline{T_s'}})$ as

$$\kappa(\lambda^2_{Z'T_s'\overline{T_s'}}) \equiv \frac{\sigma}{\sigma_{\mathrm{NWA}}}. \tag{4}$$

With the ansatz function

$$\kappa(\lambda^2_{Z'T_s'\overline{T_s'}}) = c_0 + c_1 \cdot \exp\left(-c_2 \lambda^2_{Z'T_s'\overline{T_s'}}\right) \tag{5}$$

we obtain

$$c_0 = 0.193(4), \quad c_1 = 0.812(4), \quad c_2 = 0.049(1) \tag{6}$$

for $M_{Z'} = 3$ TeV, $M_{T_s'} = 1.2$ TeV (cf. the grey dashed curve in Fig. 7 for the quality of the fit). For different mass choices, these fitting coefficients will vary due to cutoff effects appearing for large $\Gamma_{Z'}$ and due to PDF effects. For a fixed mass pair, however, $\kappa(\lambda^2_{Z'T_s'\overline{T_s'}})$ can be used universally in the $(\lambda_{Z'T_s'\overline{T_s'}}, \lambda_{Z'q\bar{q}})$ coupling space. Therefore, whenever the NWA is used in the following chapters, we rescale

$$\sigma_{\mathrm{NWA}} \mapsto \sigma_{\mathrm{NWA}} \cdot \kappa_{(M_{Z'}, M_{T_s'})}(\lambda^2_{Z'T_s'\overline{T_s'}}), \tag{7}$$

with the fitting function $\kappa_{(M_{Z'}, M_{T_s'})}(\lambda^2_{Z'T_s'\overline{T_s'}})$, determined as shown above.

One should note that finite width effects of the T_s' also can be potentially important as pointed in [71], however this is not the case for our study: (a) for $\lambda_{\phi T_s' t} = 1$ which we chose as a benchmark from now on the $\Gamma_{T_s'}$ is quite low: $\Gamma_{T_s'}/M_{T_s'} \simeq 0.01$; (b) also, in the parameter space allowed by DM constraints (see Fig. 1), $M_{T_s'}$ is far enough from $m_\phi + m_t$ kinematical limit and $M_{T_s'}$ is below 1.5 TeV. Therefore, according to [71], the respective finite width effects can be neglected for the parameter space we study. For $\lambda_{\phi T_s' t} < 1$ this is even more true since the width scales as $\lambda^2_{\phi T_s' t}$. For $\lambda_{\phi T_s' t} > 1$, finite width effects could become relevant in some small region of the parameter space where, e.g., $\lambda_{\phi T_s' t} \simeq 3$ gives $\Gamma_{T_s'}/M_{T_s'} \simeq 0.1$, which could lead to corrections of the order of 10% in the cross section. However, one cannot expect effects much larger than this, since the value of $\lambda_{\phi T_s' t}$ is bounded above by the DM DD constraints as partly demonstrated in Fig. 1.

D. QCD-only T_s' pair production

With the results of our prestudies in place, we turn to constraints on the simplified model from current LHC searches at 13 TeV. For each parameter point (with the parameter grid to be defined below), we simulate 50 000

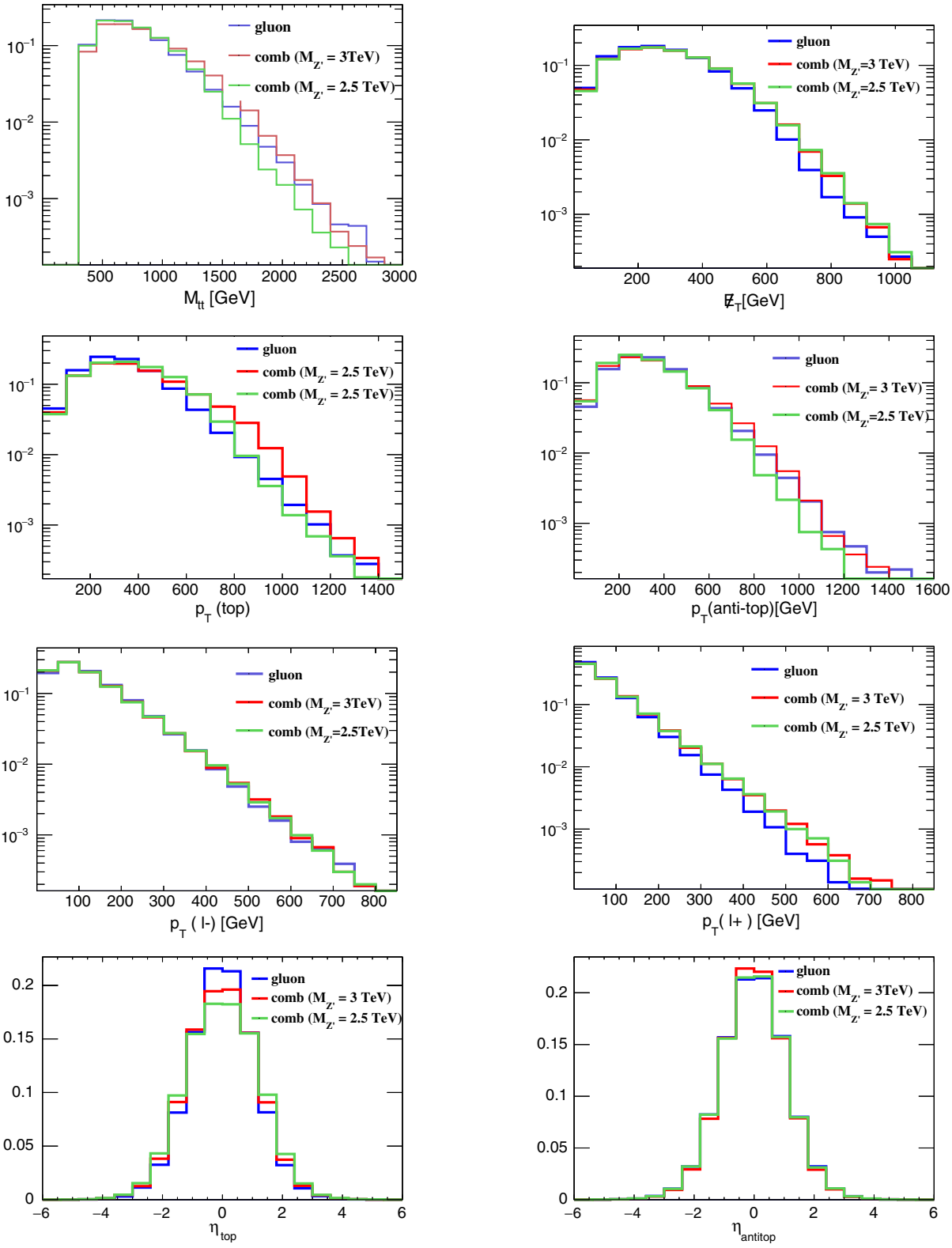

FIG. 6. Differential distributions (normalized to one) specifically for the chiral choice LL, when top partner-pair production occurs via QCD and for the combined production, i.e., QCD + Z', for $M_{Z'} = 2.5$ and 3 TeV. The produced top partners are allowed to decay to top quarks and dark matter. Distributions from QCD-only production are shown in green, the combined production for $M_{Z'} = 2.5$ TeV in blue and for $M_{Z'} = 3$ TeV in red. Here, $\lambda_{Z'T_s'\overline{T}_{s,L}'} = 2.5$, $\lambda_{Z'q\bar{q},L} = 0.25$, $M_{T_s'} = 1$ TeV and $m_\phi = 500$ GeV.

TABLE I. Cross sections for T'_s pair production for different production channels with $M_{Z'} = 2.5$ TeV. The difference is computed as "combined—(Z' + gluon)" and the relative difference as "$1 - \frac{Z'+\text{gluon}}{\text{combined}}$".

$\Gamma_{Z'}$ [GeV]	Production channel	σ [fb]	diff. [fb]	(rel. diff.) ([%])
70.5	Z'	30.9	+1.6	(+2.5%)
	QCD	32.4		
	Combined	64.9		
1134	Z'	31.3	+2.4	(+3.6%)
	QCD	32.5		
	Combined	66.2		

events which are used to compare against ATLAS and CMS searches [48–59] which are implemented in CheckMATE [72].

We first determine the limits for QCD-only T'_s-pair production (see Fig. 3, bottom), which only depend on $M_{T'_s}$ and m_ϕ, since the kinematics and the rate for the process are completely fixed by these two masses. In Fig. 8, we show the production cross section (simulated at leading order) for the QCD-only T'_s-pair production as a function of $M_{T'_s}$ together with the experimental limits for different dark matter masses m_ϕ. Using CheckMATE, we have found the strongest observed bound at 95% confidence level out of all implemented analyses with the r-value given as [47]

$$r = \frac{S - 1.64 \cdot \Delta S}{S95},$$

where S is the number of predicted signal events with its uncertainty ΔS and $S95$ is the experimental 95% upper limit on the number of signal events.

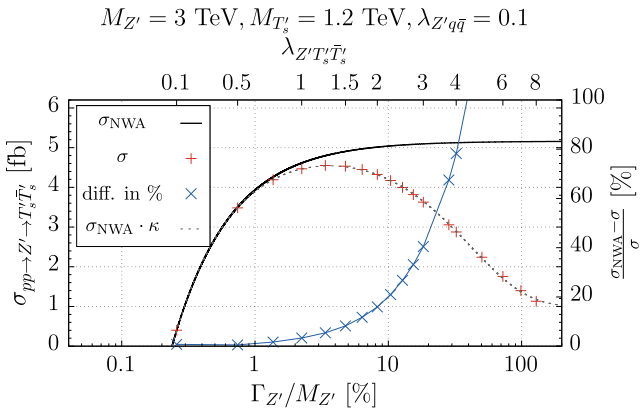

FIG. 7. Comparison of $pp \to Z' \to T'_s\bar{T}'_s$ in the NWA (black line) and without (red '+') for $M_{Z'} = 3$ TeV. The blue crosses show the difference in % between the two based on σ. The blue curve shows the fitting function Eq. (5) with fit parameters given in Eq. (6).

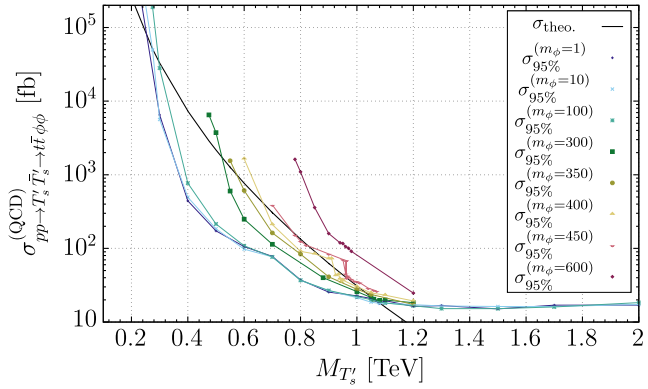

FIG. 8. Theoretical (black) and experimental (colored) cross sections for $pp \to T'_s\bar{T}'_s \to t\bar{t}\phi\phi$ in fb without Z' mediation in dependence of $M_{T'_s}$ and m_ϕ. m_ϕ is given in GeV.

It turns out that almost all limits are coming from the analysis ATLAS_CONF_2016_050 [58], a search aimed at top squarks in final states together with one isolated lepton, jets and $\not{E}_T$ at $\sqrt{s} = 13$ TeV. The most sensitive signal regions are tN_high and SR1, where the first (latter) one is aimed at high (low) mass splittings between $\tilde{t}_1$ and $\tilde{\chi}_1^0$. A large mass split results in highly boosted top quarks, whereas a small mass split is responsible for all decay products to be fully resolved [58]. For a very small mass split between $M_{T'_s}$ and m_ϕ just above the top quark threshold, i.e., when $M_{T'_s} \gtrsim m_t + m_\phi$, the analysis ATLAS_1604_07773 [50] yields the best limits. For heavy T'_s between 1.2 and 2 TeV, the experimental limits are almost constant for any m_ϕ, as the top quarks will now always be heavily boosted. The theoretically predicted signal, however, stays well below the exclusion range due to the high suppression of cross section coming from the heavy T'_s-pair. For $M_{T'_s} \approx 1.08$ TeV, the signal is excluded for all m_ϕ up to ≈300 GeV and stays excluded up to a lower bound, where $M_{T'_s} \gtrsim m_t + m_\phi$. Reducing $M_{T'_s}$ further results in off-shell top quarks with highly different kinematical distributions not studied in this work. Increasing m_ϕ beyond 300 GeV shrinks the excluded $M_{T'_s}$ region and eventually closes it for $m_\phi \gtrsim 450$ GeV, leaving all $M_{T'_s}$ allowed.

It is also worth noticing that for $m_\phi = 400$ and 450 GeV, there are small regions of nonexcluded $M_{T'_s}$ in the otherwise excluded area (e.g., at $M_{T'_s} \approx 900$ GeV). These are not actually physical, but rather correspond to a gap in the regions of parameter space the signal regions tN_high and SR1 are able to cover. For example $m_\phi = 400$ GeV and $M_{T'_s} \lesssim 920$ GeV, ATLAS_CONF_2016_050 [58] is sensitive to the signal in SR1, whereas it is most sensitive in tN_high for $M_{T'_s} \gtrsim 920$ GeV. As both signal regions do not overlap entirely, a gap in form of a kink or step is seen in the experimental cross section.

With these Z'-independent constraints on T'_s-pair production, we now investigate the current experimental di-jet

and di-lepton limits in the $(\lambda_{Z'T_s'\overline{T_s'}}, \lambda_{Z'q\bar{q}})$ plane for $M_{T_s'} \geq 1.1$ TeV, which are generally safe for any m_ϕ.

E. Di-jet and di-lepton constraints

Before further examining the model, we check which parts of the $(\lambda_{Z'T_s'\overline{T_s'}}, \lambda_{Z'q\bar{q}})$ coupling space are already excluded by current experimental di-jet and di-lepton limits. We also require the width of the Z' boson to be not excessively large, such that

$$\Gamma_{\text{tot}}(Z') < \frac{M_{Z'}}{2}, \tag{8}$$

which also ensures that Z' couplings to fermions are perturbative and one can trust our tree-level study. The total two-body Z' decay width is:

$$\Gamma_{\text{tot}}(Z') = \frac{1}{8\pi M_{Z'}^2} \sum_{\text{final states}} |\mathcal{M}|^2 |p_1| \tag{9}$$

with the 4-momentum of the first final-state particle

$$|p_1| = \frac{\sqrt{[M_{Z'}^2 - (m_1+m_2)^2][M_{Z'}^2 - (m_1-m_2)^2]}}{2M_{Z'}} = \begin{cases} \frac{\sqrt{M_{Z'}^2 - 4m^2}}{2} & , m_1 = m_2 \equiv m \\ \frac{M_{Z'}}{2} & , m_1 = m_2 = 0 \end{cases} \tag{10}$$

and already having integrated over the solid angle of the first final-state particle $\int \mathrm{d}\Omega = \iint \sin(\theta_1)\mathrm{d}\theta_1 \mathrm{d}\phi_1 = 4\pi$. The squared matrix element for a Z' decaying to quark, T_s' and lepton pairs times $|p_1|$ then reads

$$\begin{aligned} \sum_{\text{final states}} |\mathcal{M}|^2 |p_1| = {} & 2 \underbrace{\left[\sum_{\{q\}} (M_{Z'}^2 - m_q^2) \cdot |p_1(m_q)| \right]}_{\equiv A_q} \lambda_{Z'q\bar{q}}^2 \\ & + \underbrace{2(M_{Z'}^2 - M_{T_s'}^2) \cdot |p_1(M_{T_s'})|}_{\equiv A_{T_s'}} \lambda_{Z'T_s'\overline{T_s'}}^2 \\ & + \underbrace{\frac{2}{3} \left[\sum_{\{\ell\}} (M_{Z'}^2 - m_\ell^2) \cdot |p_1(m_\ell)| \right]}_{\equiv A_\ell} \lambda_{Z'\ell^+\ell^-}^2 . \end{aligned} \tag{11}$$

Plugging Eq. (11) into Eqs. (9) and (8) yields a combined upper bound on $\lambda_{Z'q\bar{q}}$, $\lambda_{Z'T_s'\overline{T_s'}}$ and $\lambda_{Z'\ell^+\ell^-}$. This bound together with the experimental limits from ATLAS and CMS for di-jet [73,74] and di-lepton [75,76] searches is shown in Figs. 9 ($\lambda_{Z'\ell^+\ell^-} = 0$) and 10 ($\lambda_{Z'\ell^+\ell^-} = \lambda_{Z'q\bar{q}}$) in detail for several combinations of $M_{Z'}$ and $M_{T_s'}$, where the limits for $\lambda_{Z'T_s'\overline{T_s'}} > 0$ were found using the NWA

$$\sigma_{pp\to Z'\to jj}(\lambda_{Z'q\bar{q}}(0)) = \sigma_{pp\to Z'}(\lambda_{Z'q\bar{q}}(\lambda_{Z'T_s'\overline{T_s'}})) \cdot \text{BR}(Z' \to q\bar{q}), \tag{12a}$$

$$\sigma_{pp\to Z'\to \ell^+\ell^-}(\lambda_{Z'q\bar{q}}(0)) = \sigma_{pp\to Z'}(\lambda_{Z'q\bar{q}}(\lambda_{Z'T_s'\overline{T_s'}})) \cdot \text{BR}(Z' \to \ell^+\ell^-), \tag{12b}$$

with $\lambda_{Z'q\bar{q}}(0)$ being the experimental limit for $\lambda_{Z'T_s'\overline{T_s'}} = 0$.

While the di-jet bounds already set rather strong limits on $\lambda_{Z'q\bar{q}}$, the di-lepton bounds extend these even more, especially at small $M_{Z'}$. With increasing $M_{Z'}$, all bounds get substantially weaker, whereas an increase of $M_{T_s'}$ is affecting the bounds only slightly. When $M_{Z'}$ is getting close to $2M_{T_s'}$ (see Figs. 9 and 10, top left and bottom right), the parameter space broadens in the $\lambda_{Z'T_s'\overline{T_s'}}$ direction due to $A_{T_s'}$ becoming small and thus allowing for larger $\lambda_{Z'T_s'\overline{T_s'}}$ to be realized.

Eventually, we find that a significant fraction of parameter space, especially for large values of $\lambda_{Z'T_s'\overline{T_s'}}$, is still available for study.

F. LHC reach including Z' bosons

After establishing constrains on the $(\lambda_{Z'T_s'\overline{T_s'}}, \lambda_{Z'q\bar{q}})$ parameter space from current di-jet and di-lepton bounds, we are ready to investigate the remaining parameter space for our $t\bar{t} + \not{E}_T$ signature. To do so, we first use `CheckMATE` to analyze 50000 events generated for the Z'-mediated part of Fig. 3 (left graph) individually for all on-shell $(M_{Z'}, M_{T_s'})$ combinations and $m_\phi = (10, 62.5, 100, 300, 600)$ GeV together with $\lambda_{Z'q\bar{q}} = 0.2$ and $\lambda_{Z'T_s'\overline{T_s'}} = 2$.

It turns out that the majority of points are constrained mostly by the `ATLAS_CONF_2016_050` [58] analysis in the `tN_high` signal region. Only for very large $M_{Z'}$ and $M_{T_s'}$, `ATLAS_1605_03814` [51] gives stronger limits in the `2jt` signal region (although being only slightly more constraining than the `ATLAS_CONF_2016_050` `tN_high` limit). Therefore, we can use the NWA once more to rescale the detection/exclusion limits computed by `CheckMATE` via

$$\sigma_{95\%} \overset{!}{=} \sigma_{\text{signal}} = \sigma_{pp\to Z'} \cdot \text{BR}(Z' \to T_s'\overline{T_s'}) = \mathcal{P}\lambda_{Z'q\bar{q}}^2 \cdot \frac{A_{T_s'}\lambda_{Z'T_s'\overline{T_s'}}^2}{A_{T_s'}\lambda_{Z'T_s'\overline{T_s'}}^2 + A_q\lambda_{Z'q\bar{q}}^2 + A_\ell\lambda_{Z'\ell^+\ell^-}^2}, \tag{13}$$

where $\sigma_{95\%}$ indicates the bound (at 95% C.L.) on the observed production cross section from the most

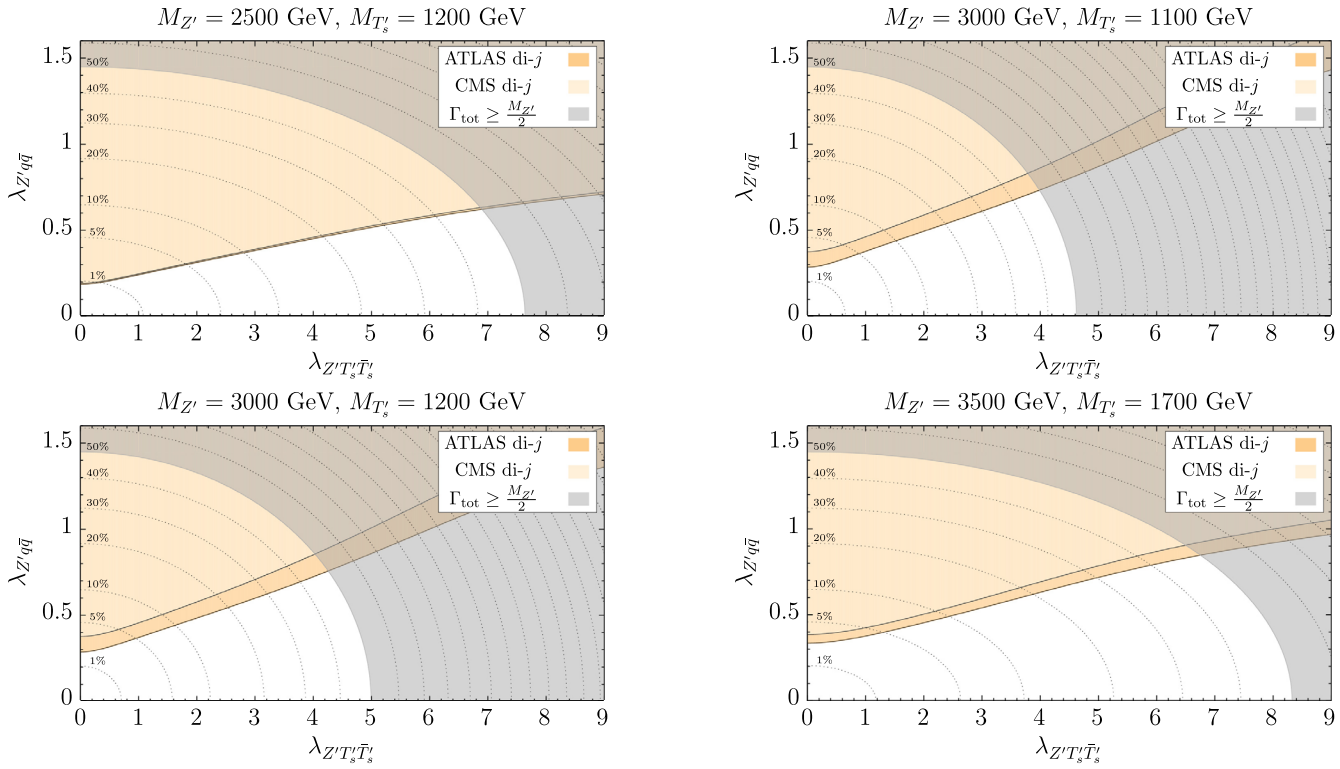

FIG. 9. $(\lambda_{Z'T'_s\overline{T}'_s}, \lambda_{Z'q\bar{q}})$ parameter space for $\lambda_{Z'\ell^+\ell^-} = 0$ and different $M_{Z'}$ and $M_{T'_s}$ with di-jet and di-lepton bounds. The dotted lines from bottom to top show when the Z' width is $(1, 5, 10, 20, \ldots)\%$ of its mass.

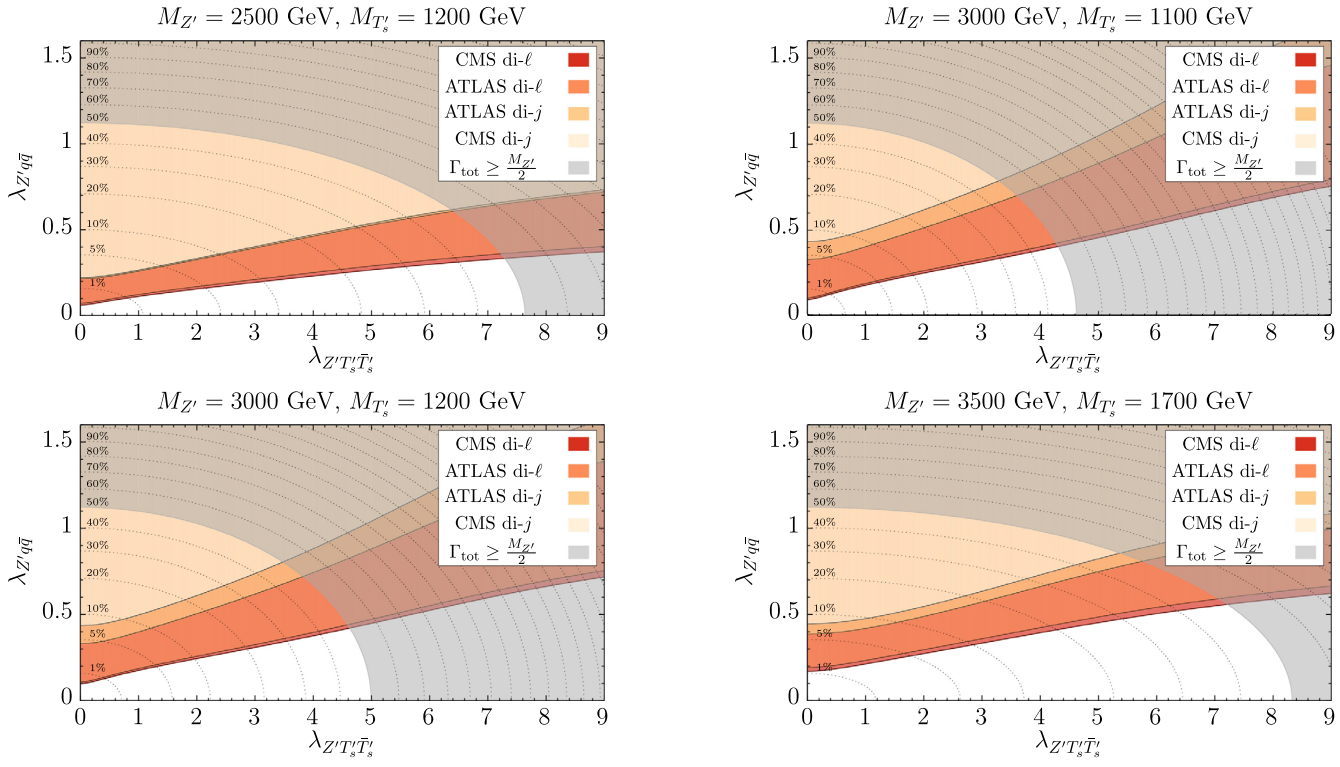

FIG. 10. $(\lambda_{Z'T'_s\overline{T}'_s}, \lambda_{Z'q\bar{q}})$ parameter space for $\lambda_{Z'\ell^+\ell^-} = \lambda_{Z'q\bar{q}}$ and different $M_{Z'}$ and $M_{T'_s}$ with di-jet and di-lepton bounds. The dotted lines from bottom to top show when the Z' width is $(1, 5, 10, 20, \ldots)\%$ of its mass.

constraining search and parameter region and $\mathcal{P} = \mathcal{P}(M_{Z'}) = \frac{\sigma_{pp\to Z'}}{\lambda^2_{Z'q\bar{q}}}$ is the prefactor of the Z' production cross section and only depends on $M_{Z'}$. This allows us to find the excluded $(\lambda_{Z'T'_s\overline{T'_s}}, \lambda_{Z'q\bar{q}})$ parameter space. An interesting set of these exclusion limits is shown in blue in Figs. 11 ($\lambda_{Z'\ell^+\ell^-} = 0$) and 12 ($\lambda_{Z'\ell^+\ell^-} = \lambda_{Z'q\bar{q}}$) for various values of m_ϕ, indicated as black solid and dashed lines at the bottom of the blue band. For large $\lambda_{Z'T'_s\overline{T'_s}}$, the $t\bar{t} + \not{E}_T$ limit is nearly saturated with respect to $\lambda_{Z'q\bar{q}}$. This is due to $\mathrm{BR}(Z' \to T'_s\overline{T'_s}) \gg \mathrm{BR}(Z' \to q\bar{q})$, ensuring a sufficient amount of T'_s-pairs surviving the experimental cuts is produced. However, as we rescale the NWA according to Eq. (7), the limits also slightly decrease for increasing $\lambda_{Z'T'_s\overline{T'_s}}$ (see, e.g., Figs. 11 and 12, top right and bottom left). On the contrary, for decreasing $\lambda_{Z'T'_s\overline{T'_s}}$, the $t\bar{t} + \not{E}_T$ limit gets maximal before abruptly vanishing soon after. This is due to $\mathrm{BR}(Z' \to T'_s\overline{T'_s}) \lesssim \mathrm{BR}(Z' \to q\bar{q})$, resulting in a suppression of T'_s-pair production. The slope or shape of that drop is mainly influenced by $\Delta M = M_{Z'} - 2M_{T'_s}$. The smaller ΔM, the more rectangular the shape will become, whereas for larger ΔM, the shape will turn smoother and rounder.

In comparison to the di-lepton and di-jet limits, the $t\bar{t} + \not{E}_T$ signature is able to cover large parts of the parameter space where T'_s-pair production gets more and more dominant (i.e., for large $\lambda_{Z'T'_s\overline{T'_s}}$), as long as $M_{Z'}$ is sufficiently small. With increasing $M_{Z'}$, the $t\bar{t} + \not{E}_T$ limit weakens substantially and gets even weaker than the di-lepton and di-jet bounds, once $M_{Z'} \geq 4$ TeV (not shown here). However, for $M_{Z'} \leq 3$ TeV, the $t\bar{t} + \not{E}_T$ limit is the most constraining one in terms of parameter space coverage, whereas the di-lepton and di-jet limits yield strong, additional constraints for very small $\lambda_{Z'T'_s\overline{T'_s}}$.

In summary, by taking into account both di-lepton and di-jet as well as the $t\bar{t} + \not{E}_T$ limits, we are able to efficiently constrain the $(\lambda_{Z'T'_s\overline{T'_s}}, \lambda_{Z'q\bar{q}})$ parameter space for most values of $\lambda_{Z'q\bar{q}}$.

G. Detailed benchmark analysis

Based on the above studies, we choose a specific benchmark point in the $(\lambda_{Z'T'_s\overline{T'_s}}, \lambda_{Z'q\bar{q}})$ plane for further detailed investigation, followed by a qualitative discussion for other coupling choices. The benchmark we choose now covers all $T'_s\overline{T'_s}$ production processes shown in Fig. 3 and covers all interesting states of exclusion, i.e., being excluded by all limits for small $M_{Z'}$, only excluded by the $t\bar{t} + \not{E}_T$ signature and not excluded at all. The benchmark comprises the following couplings [77]

$$\lambda_{Z'q\bar{q}} = 0.25, \quad \lambda_{Z'T'_s\overline{T'_s}} = 2.5, \quad \lambda_{Z'\ell^+\ell^-} = \lambda_{Z'q\bar{q}}, \tag{14}$$

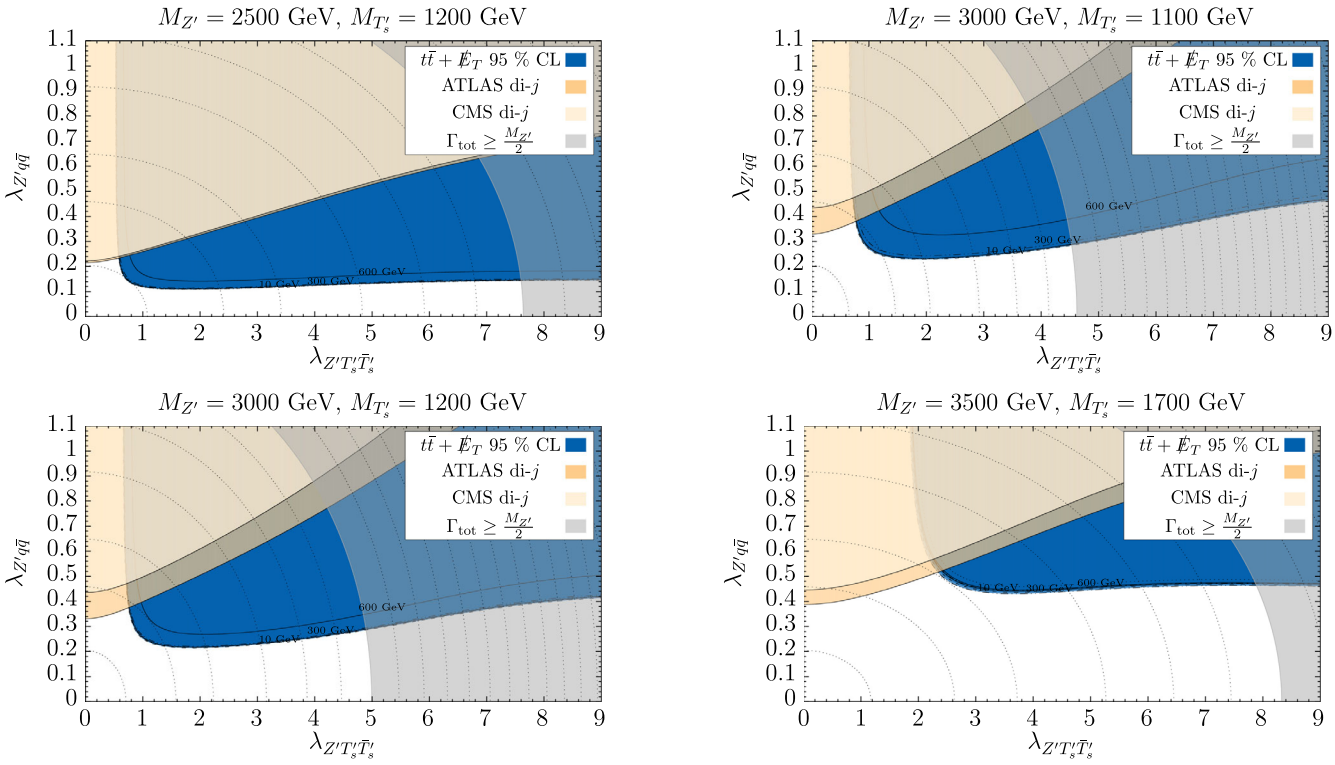

FIG. 11. Di-jet and di-lepton bounds together with the most constraining $t\bar{t} + \not{E}_T$ bounds coming from ATLAS_CONF_2016_050 for $\lambda_{Z'\ell^+\ell^-} = 0$. The parameter space below the colored bands is not excluded and available for study. The labels "10", "300" and "600" on the black lines refer to m_ϕ in GeV for the blue $t\bar{t} + \not{E}_T$ bound.

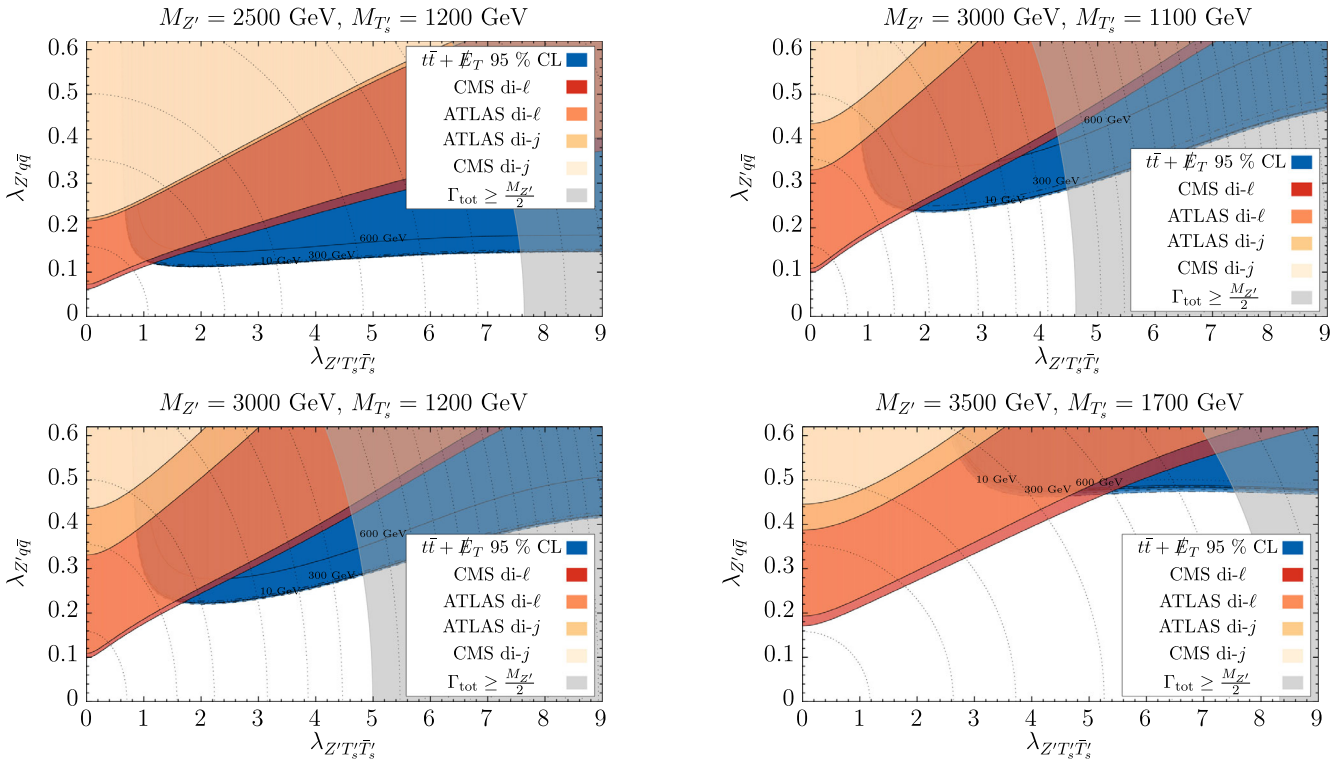

FIG. 12. Di-jet and di-lepton bounds together with the most constraining $t\bar{t} + \not{E}_T$ bounds coming from ATLAS_CONF_2016_050 for $\lambda_{Z'\ell^+\ell^-} = \lambda_{Z'q\bar{q}}$. The parameter space below the colored bands is not excluded and available for study. The labels "10", "300" and "600" on the black lines refer to m_ϕ in GeV for the blue $t\bar{t} + \not{E}_T$ bound.

and an overview over all related cross sections in the studied $M_{Z'}$-$M_{T'_s}$ range can be found in Fig. 13.

Therein, the top three numbers from left to right in each rectangle correspond to the experimental limits for $m_\phi =$ 10, 300, 600 GeV, respectively, whereas the number in the center corresponds to our signal cross section and coincides with the color coding. By pinning down the benchmark-couplings in the $(\lambda_{Z'T'_s\overline{T}'_s}, \lambda_{Z'q\bar{q}})$ plane from Figs. 11 and 12 and then comparing with the numbers from Fig. 13, it is clear that the mass pairs $(M_{Z'}, M_{T'_s}) = (2.5, 1.2)$ TeV and

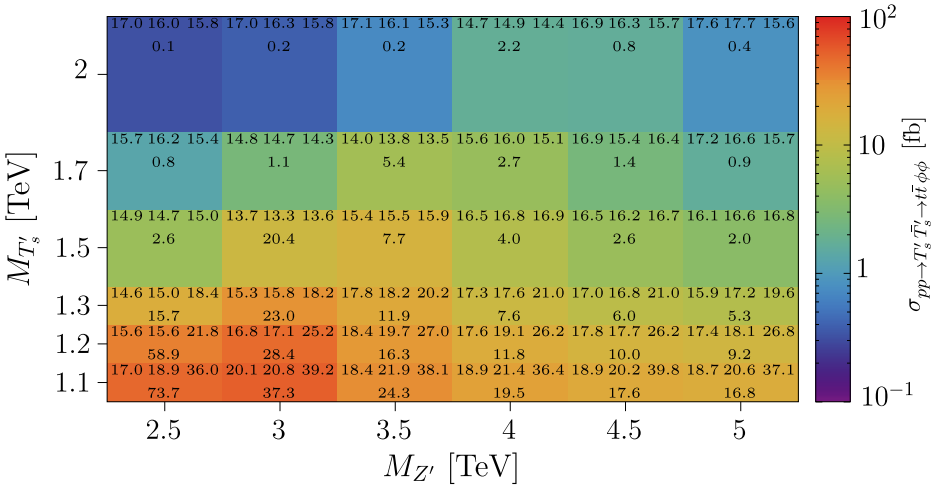

FIG. 13. Predicted cross sections for $pp \to T'_s\overline{T}'_s \to t\bar{t}\phi\phi$ in fb in dependence of $M_{Z'}$ and $M_{T'_s}$. The top three numbers in a rectangle from left to right show the experimental limit on the cross section in fb for $m_\phi = 10$, 300, 600 GeV, respectively, whereas the number below shows the theoretical prediction coinciding with the color coding. The couplings are chosen as $\lambda_{Z'q\bar{q}} = 0.25 = \lambda_{Z'\ell^+\ell^-}$ and $\lambda_{Z'T'_s\overline{T}'_s} = 2.5$.

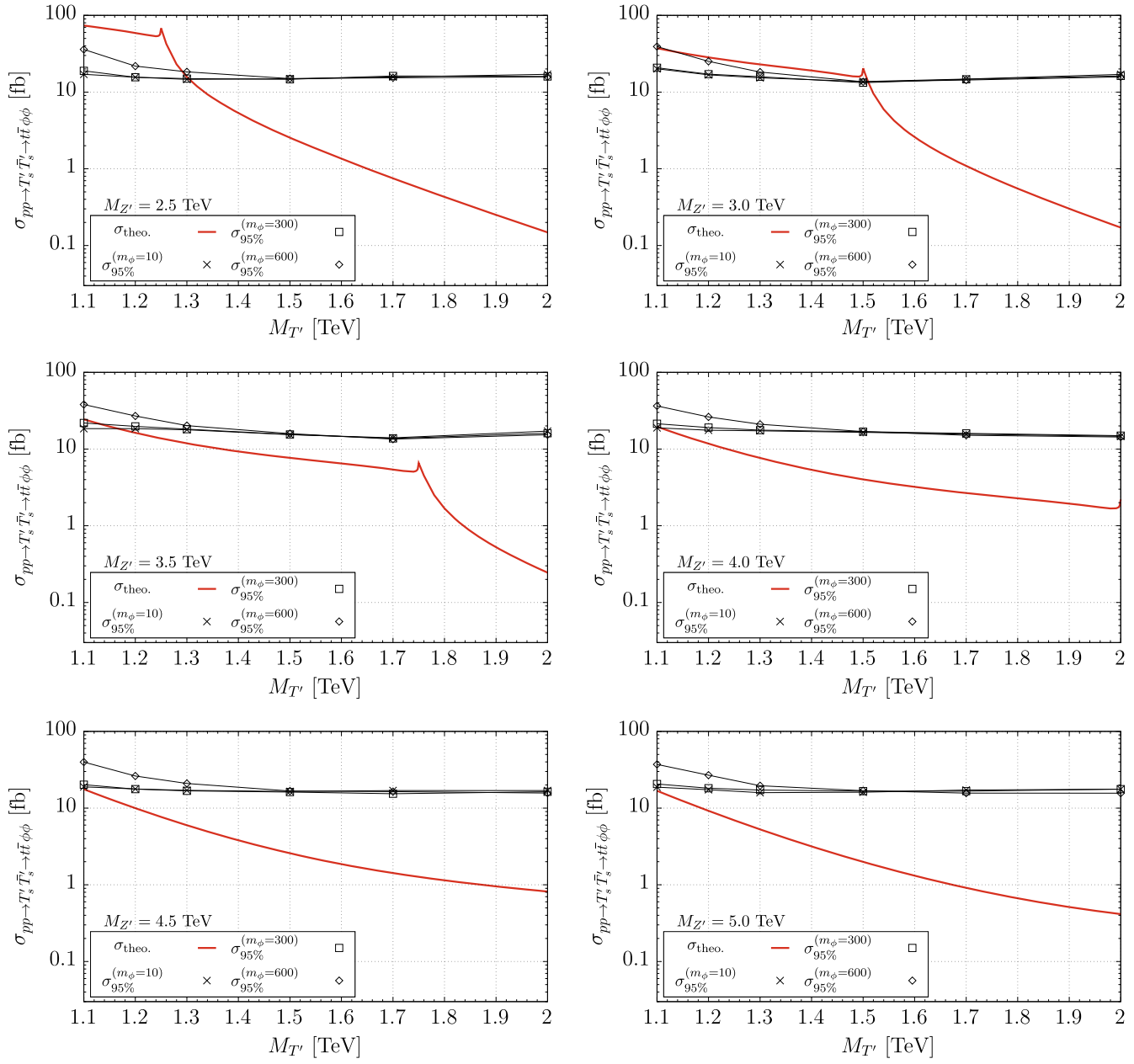

FIG. 14. Theoretical (red) and experimental (black) cross sections for $pp \to T'_s\overline{T'_s} \to t\bar{t}\phi\phi$ in fb in dependence of $M_{T'_s}$ and M_ϕ for our benchmark point (same data as in Fig. 13). M_ϕ is given in GeV and the couplings read $\lambda_{Z'q\bar{q}} = 0.25 = \lambda_{Z'\ell^+\ell^-}$ and $\lambda_{Z'T'_s\overline{T'_s}} = 2.5$.

(3,1.2) TeV are strongly excluded, even without the QCD contributions to T'_s-pair production. For (3.5,1.7) TeV, neither the full nor the Z'-only limit is able to probe that point, due to the predicted cross section being too small because of the large $M_{Z'}$ and $M_{T'_s}$.

To get a better idea about the experimental and signal cross sections, the same data as in Fig. 13 have been plotted again in Fig. 14, but this time for constant $M_{Z'}$, variable $M_{T'_s}$ and m_ϕ up to 600 GeV. The red curves show the signal cross section, whereas the black symbols correspond to the experimental cross section for $m_\phi = 10$, 300, 600 GeV, respectively.

In comparison to Fig. 13, it is now possible to spot the signal exclusion for each $M_{Z'}$ more easily. For $M_{Z'} = 2.5$ TeV, the signal is excluded up to $M_{T'_s} \approx 1.3$ TeV, therefore excluding the entire regime for on-shell T'_s-pair production. For $M_{Z'} = 3$ TeV, the results are similar, although the exclusion now starts at roughly $M_{T'_s} = 1.51$ TeV, just after off-shell production starts. With $M_{Z'} = 3.5$ TeV, the Z' contributions to the predicted cross sections start to weaken with most of the on-shell regime not being excluded (up to $M_{T'_s} = 1.16$ TeV). For larger $M_{Z'}$, the Z' contributions are too small to yield any new exclusion limit and all signal curves are excluded for

$M_{T_s'} = 1.08$ TeV, the limit from pure QCD T_s'-pair production as shown in Fig. 8.

As mentioned above, this analysis only holds in that amount of detail for the chosen benchmark $(\lambda_{Z'q\bar{q}}, \lambda_{Z'T_s'\overline{T_s'}}) = (0.25, 2.5)$. It is possible, however, to do a qualitative analysis also for different benchmarks. For that, we note again that slight changes in $\lambda_{Z'T'\overline{T_s'}}$ will not significantly change the cross section (see blue, approximately horizontal limits in Fig. 12), which can be explained in the scope of the NWA by the saturation of $\mathrm{BR}(Z' \to T_s'\overline{T_s'}) \to 1$ for increasing $\lambda_{Z'T_s'\overline{T_s'}}$ (see Sec. III F). The cross section will drop, however, once the NWA is not applied, and we took this drop into account by rescaling the NWA cross sections by a fitting function $\kappa(\lambda^2_{Z'T_s'\overline{T_s'}})$. Still, the drop in cross section is rather small for changing $\lambda_{Z'T_s'\overline{T_s'}}$ and will therefore just slightly influence the limits obtained when performing a full benchmark study. When changing $\lambda_{Z'q\bar{q}}$, on the other hand, the situation changes significantly. Increasing $\lambda_{Z'q\bar{q}}$ will lead to rapidly growing cross sections and therefore a rapid shift of the limits as well, whereas the inverse holds for decreasing $\lambda_{Z'q\bar{q}}$.

Since we have positive interference between the Z' and QCD T_s'-pair production channels (see Sec. III B), we are also able to give an idea about the excluded $M_{T_s'}$ range for different benchmarks based on the above qualitative discussion. As can be seen in Fig. 8, for $M_{T_s'} \gtrsim 1.2$ TeV, the QCD contributions only make up for about half of the experimental bound. Since including the Z' channel with $M_{Z'} \leq 3$ TeV leads to an exclusion of the signal (see Fig. 14), we can deduct that the Z' parts clearly dominate the signal and an increase in $\lambda_{Z'q\bar{q}}$ would only enhance this behavior. For heavier Z' up to 5 TeV, the Z' and QCD channels are contributing nearly identical parts to the cross section. Not enough, however, to exceed the experimental bounds.

The above argument is also true for $M_{T_s'} \gtrsim m_t + m_\phi$ up to $M_{T_s'} \approx m_t + m_\phi + \mathcal{O}(50\ \mathrm{GeV})$ (see Fig. 8, left ends of colored lines), as long as $m_\phi \lesssim 450\,\mathrm{GeV}$ and $M_{Z'} \leq 3$ TeV. For the remaining $M_{T_s'}$ between $m_t + m_\phi + \mathcal{O}(50\ \mathrm{GeV})$ and 1.2 TeV, it is hard to give any qualitative statement due to the strong signal dependence of m_ϕ and a dedicated benchmark analysis as the one we performed above needs to be done.

Returning to the benchmark set of couplings presented in this subsection, let us put our results into context with the dark matter bounds presented in Sec. II. In analogy to the green LHC no-Z' bounds from Figs. 1 and 2, we are now presenting these limits for our benchmark including Z' and demonstrate its role. The bounds for the no-Z' case and for $M_{Z'} = 2.5$ and 3 TeV are shown in Fig. 15 together with the relic density for $\lambda_{\phi H} = 0$ and $\lambda_{\phi T_s' t} = 1$.

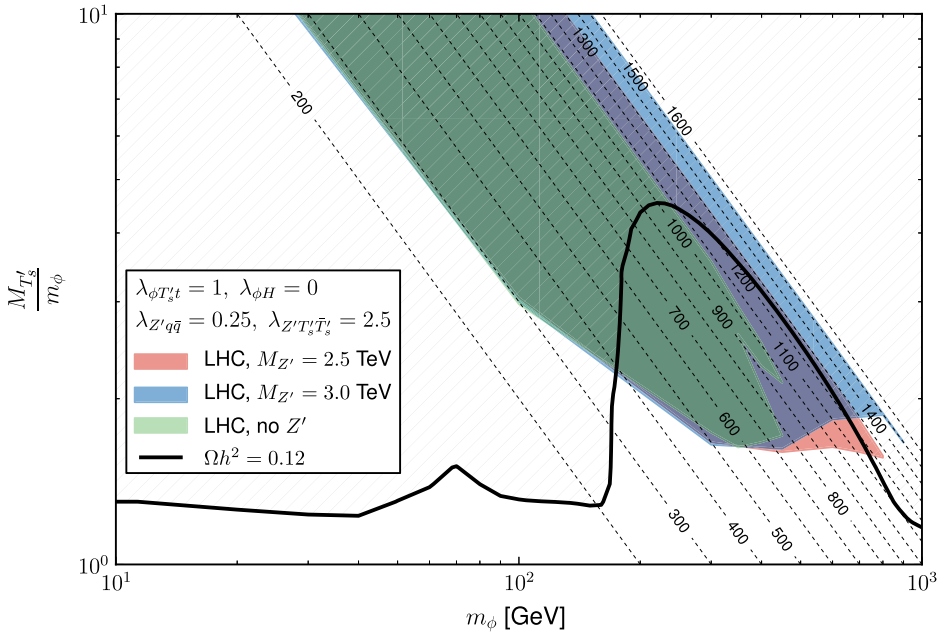

FIG. 15. LHC, DM Direct Detection and relic density constraints on the parameter space of the ZP-TP-DM model in the $\left(\frac{M_{T_s'}}{m_\phi}, m_\phi\right)$ plane for $\lambda_{\phi H} = 0$ and $\lambda_{\phi T_s' t} = 1$: a) the green-shaded area indicates the current LHC exclusion region for the $t\bar{t} + \not{E}_T$ signature coming from the process $pp \to T_s'\overline{T_s'} \to t\bar{t}\phi\phi$, mediated by gluon exchange only (no Z'); b) the red- and blue-shaded areas present the extended reach of the LHC for $M_{Z'} = 2.5$ and 3 TeV, respectively, with $\lambda_{Z'q\bar{q}} = 0.25 = \lambda_{Z'\ell^+\ell^-}$ and $\lambda_{Z'T_s'\overline{T_s'}} = 2.5$; c) the grey-hatched parameter space above the black contour is excluded by relic density constraints. The thin dashed lines with the respective labels indicate the iso-levels of $M_{T_s'}$ in GeV.

While the green limits without Z' already cover a large fraction of parameter space up to $m_\phi = 450$ GeV, including the Z' contributions allows us to extend this range up to $m_\phi = 800(900)$ GeV for $M_{Z'} = 2.5(3)$ TeV, therefore completely closing the gap between LHC and relic density constraints along the m_ϕ axis. For $M_{Z'} \geq 3.5$ TeV, the Z' contributions are too small to enhance the limits visibly (see Fig. 14, middle and bottom row) and the QCD-only limits become maximal again.

To give a general idea about the kinematic properties for different $(M_{T'_s}, m_\phi)$ mass pairs in the studied region, we also present four more sub-benchmarks and their QCD-only contributions in Tables II and III in the Appendix. The CheckMATE cut flow in the lower part of the Tables shows the fraction of events surviving the listed cut (normalized to 1). The last row in the cut-flow section (bold) therefore corresponds to the overall efficiency. The impact of the Z' can be estimated by comparing the efficiencies between benchmarks in Tables II and III. In Table II, we also present the cut-flow efficicency for the BP2-RR benchmark, which is analogue to the BP2 benchmark, but with the RR Z' coupling combination. One can see that the efficiencies for LL (BP2 benchmark) and RR (BP2-RR benchmark) differ only by about 2%. At the same time, the overall efficiencies for the "QCD" benchmarks from Table III and benchmarks with Z' from Table II differ by 10%–15%, which is not negligible. This difference in efficiencies is related to an obvious difference in the kinematics between the QCD and Z'-mediated processes: a) the rapidity of a $T'_s\overline{T'_s}$-pair originating from a Z' is broader than from QCD production, since the Z' is produced from $q\bar{q}$ fusion; b) the $\not{E}_T$ distribution is harder when Z' bosons are included, especially for heavier Z' bosons; c) top partners are more boosted in case of Z' mediation, which makes final state leptons more energetic but less isolated.

IV. CONCLUSIONS

We have explored the phenomenology of a simplified, effective model with a vector resonance Z', a fermionic vectorlike colored partner of the top quark T', which carries negative DM parity, and a scalar DM candidate ϕ—which we refer to as the ZP-TP-DM model. The particle content of this effective model appears as part of the spectrum in several classes of models, including composite Higgs models, little Higgs models, and Randall-Sundrum models (if equipped with a DM candidate).

Our main focus is the exploration of the process $pp \to Z' \to T'\overline{T'} \to t\bar{t}\phi\phi$ at the LHC, which to the best of our knowledge has not been studied previously. The final state resembles the final state of SUSY stop pair production final states, and we recasted ATLAS and CMS searches which are implemented in CheckMATE in order to determine to what extent the ZP-TP-DM model is covered by existing searches. We have found that the $pp \to Z' \to T'\overline{T'} \to t\bar{t}\phi\phi$ process plays an important role in addition to the $T'\overline{T'}$ production via QCD interactions.

Because the process under study originates exclusively from a quark-antiquark initial state and because the $T'\overline{T'}$-pair arises from an on-shell Z' decay, its kinematical behavior is quite different from QCD $T'\overline{T'}$-pair production. On the one hand, the Z'-mediated $t\bar{t}\phi\phi$ signature leads to higher p_T leptons and $\not{E}_T$ (especially for heavier Z') compared to the case of QCD production alone, but on the other hand, leptons for the Z'-mediated process have higher rapidity. These two features affect the detector efficiency for the signature in opposite ways—the higher p_T of leptons and the higher $\not{E}_T$ increase efficiency, while the higher rapidity of the leptons decreases it. The overall effect is that the detector efficiency for the Z'-mediated $t\bar{t}\phi\phi$ signature is about 10% higher then for the QCD-mediated one. We showed that the chirality of the Z' couplings to SM quarks and to top partners do not play a major role in kinematical distributions, and therefore similar efficiencies apply for all chiral combinations of couplings. We also explored the effect of interference between the Z' and QCD initiated processes and have found that the interference is positive, but very small—at the level of about +3% and essentially independent of the Z' width.

We have found that the presence of the Z' can provide an additional and even dominant contribution (about 1 order of magnitude larger than the QCD one) to the $t\bar{t}\phi\phi$ signature without conflicting with existing bounds from Z' searches in di-jet and di-lepton final states. We have demonstrated that the $t\bar{t} + \not{E}_T$ signature at the LHC plays an important and complementary role to noncollider searches in setting the limits on the ZP-TP-DM parameter space. Moreover, the Z', T' and DM masses can be probed with the $t\bar{t} + \not{E}_T$ signature well beyond the reach of QCD production alone, without being in conflict with existing Z' search bounds from di-lepton and di-jet signatures, as we explicitly showed. From Fig. 15, one can see that with $M_{Z'} = 3$ TeV, the LHC is already probing DM masses up to about 900 GeV and $M_{T'}$ up to about 1.5 TeV, which is about a factor of 2 larger (for both particles) than for the bounds from QCD production alone. We regard this potential increase in reach quite remarkable and think that it is worth considering Z'-mediated top partner-pair production in future phenomenological studies and experimental searches.

We provide publicly available implementations of the model at HEPMDB [38] under hepmdb:0717.0253 [39] (CalcHEP) and hepmdb:0717.0254 [40] (Madgraph) and we would like to encourage experimental groups at the LHC to explore the potential of Z'-mediated top partner pair-production followed by their decays to dark matter.

In this study, we focussed on a region in parameter space with $M_{T'} - m_\phi > m_t$, i.e., the case in which the decay of a top partner into a top quark and DM occurs on-shell. The case of strongly degenerate $M_{T'}$ and m_ϕ, where the top

partner only decays off-shell, is not covered by the analysis presented here, but we would like to point out that in this case, a study similar to the case of SUSY with degenerate stops and neutralinos can be performed.

ACKNOWLEDGMENTS

The authors would like to thank Alexander Pukhov for discussions and finding and fixing a bug in the MICROMEGAs package which was crucial in order to produce the correct results for the DM direct detection rates for the model under study. The authors acknowledge the use of the IRIDIS High Performance Computing Facility, and associated support services at the University of Southampton, in the completion of this work. A. S. B. and P. B. S. acknowledge partial support from the InvisiblesPlus RISE from the European Union Horizon 2020 research and innovation program under the Marie Sklodowska-Curie Grant Agreement No. 690575. A. S. B. also thanks the NExT Institute, Royal Society Leverhulme Trust Senior Research Fellowship LT140094 and Soton-FAPESP grant for partial support. T. F.'s work was supported by IBS under the project code IBS-R018-D1. The work of B. J. was partially supported by the São Paulo Research Foundation (FAPESP) under Grants No. 2016/01343-7 and No. 2017/05770-0.

APPENDIX: BENCHMARK CUT FLOWS

The following Tables hold four benchmarks for the full process shown in Fig. 3 (Table II) and for the QCD-only production (Table III) together with the respective cut flows for each benchmark. The couplings of all benchmark points read $\lambda_{Z'q\bar{q}} = \lambda_{Z'\ell^+\ell^-} = 0.25$, $\lambda_{Z'T'_s\overline{T'_s}} = 2.5$, $\lambda_{\phi H} = 0$ and $\lambda_{\phi T'_s t} = 0.1$. Additionally, we provide the benchmark "BP2-RR", which is the chiral counterpart to the LL choice we used throughout this work (see Sec. III A) and has $\lambda_{Z'q\bar{q},R} = \lambda_{Z'\ell^+\ell^-,R} = 0.25$, $\lambda_{Z'T'_s\overline{T'_s},R} = 2.5$ and $\lambda_{Z'q\bar{q},L} = 0 = \lambda_{Z'\ell^+\ell^-,L}$, $\lambda_{Z'T'_s\overline{T'_s},L} = 0$.

TABLE II. Benchmarks for the full process (see Fig. 3) together with the CheckMATE cut-flow efficiencies (fraction of events surviving a certain cut, normalized to 1). The couplings for all points read $\lambda_{Z'q\bar{q}} = \lambda_{Z'\ell^+\ell^-} = 0.25$, $\lambda_{Z'T'_s\bar{T}'_s} = 2.5$, $\lambda_{\phi H} = 0$ and $\lambda_{\phi T'_s t} = 0.1$. The cut flow corresponds to the SR tN_high from ATLAS_CONF_2016_050, which yields the best limits.

	Parameter	BP1	BP2	BP2-RR	BP3	BP4
INPUT	$M_{Z'}$ [GeV]	2500	3000	3000	3000	3500
	$M_{T'_s}$ [GeV]	1150	1200	1200	1500	1700
	m_ϕ [GeV]	600	300	300	300	500
	$\Gamma_{Z'}$ [GeV]	241.75	435.61	435.61	59.61	227.40
	$\frac{\Gamma_{Z'}}{M_{Z'}}$ [%]	16.11	14.52	14.52	1.99	6.50
	σ [fb]	66.24	28.29	28.29	20.46	5.40
CUT FLOW	0_trigger_etmiss	0.81518	0.90046	0.89952	0.92820	0.93820
	1_lepton_onelepton	0.17616	0.18460	0.18678	0.18566	0.18072
	2_mt	0.17184	0.17992	0.18190	0.18166	0.17734
	3_jets	0.16436	0.16782	0.17030	0.17042	0.16630
	tN_high_01_tauVeto	0.14892	0.15640	0.15716	0.16108	0.15782
	tN_high_02_nJets	0.08944	0.08940	0.09160	0.08970	0.08618
	tN_high_03_JetsPT	0.07292	0.07766	0.07934	0.08020	0.07594
	tN_high_04_etmiss	0.03268	0.05156	0.05208	0.06118	0.06030
	tN_high_05_etmissVcal	0.03268	0.05156	0.05208	0.06118	0.06030
	tN_high_06_htmiss	0.03250	0.05118	0.05162	0.06092	0.05970
	tN_high_07_mt	0.02930	0.04672	0.04706	0.05612	0.05526
	tN_high_08_amt2	0.02872	0.04578	0.04626	0.05542	0.05456
	tN_high_09_no	0.02872	0.04578	0.04626	0.05542	0.05456
	tN_high_10_no	0.02872	0.04578	0.04626	0.05542	0.05456
	tN_high_11_dR	0.02638	0.04082	0.04046	0.05090	0.04934
	tN_high_12_LRJET_PT	0.02354	0.03846	0.03808	0.04888	0.04766
	tN_high_13_LRJET_M	0.02146	0.03530	0.03480	0.04580	0.04412
	tN_high_14_dphi	**0.02030**	**0.03334**	**0.03250**	**0.04272**	**0.04104**

TABLE III. QCD benchmarks (see Fig. 3, center and right) together with the CheckMATE cut-flow efficiencies (fraction of events surviving a certain cut, normalized to 1). The couplings for all points read $\lambda_{Z'q\bar{q}} = \lambda_{Z'\ell^+\ell^-} = 0.25$, $\lambda_{Z'T_s'\bar{T}_s'} = 2.5$, $\lambda_{\phi H} = 0$ and $\lambda_{\phi T_s' t} = 0.1$. The cut flow corresponds to the SR tN_high from ATLAS_CONF_2016_050, which yields the best limits.

	Parameter	BP1-QCD	BP2-QCD	BP3-QCD	BP4-QCD
Input	$M_{Z'}$ [GeV]	...	...	...	...
	$M_{T_s'}$ [GeV]	1150	1200	1500	1700
	m_ϕ [GeV]	600	300	300	500
	$\Gamma_{Z'}$ [GeV]	...	...	...	...
	$\frac{\Gamma_{Z'}}{M_{Z'}}$ [%]	...	...	...	...
	σ [fb]	11.62	8.49	1.49	0.51
Cut flow	0_trigger_etmiss	0.81470	0.88948	0.93012	0.93932
	1_lepton_onelepton	0.17338	0.18490	0.17670	0.17674
	2_mt	0.16814	0.17936	0.17280	0.17274
	3_jets	0.15880	0.16744	0.16024	0.15952
	tN_high_01_tauVeto	0.14244	0.15376	0.15060	0.15032
	tN_high_02_nJets	0.09092	0.09196	0.08616	0.08528
	tN_high_03_JetsPT	0.07704	0.08022	0.07682	0.07574
	tN_high_04_etmiss	0.03576	0.05076	0.05804	0.05862
	tN_high_05_etmissVcal	0.03576	0.05076	0.05804	0.05862
	tN_high_06_htmiss	0.03550	0.05028	0.05714	0.05772
	tN_high_07_mt	0.03136	0.04468	0.05164	0.05316
	tN_high_08_amt2	0.03036	0.04368	0.05060	0.05240
	tN_high_09_no	0.03036	0.04368	0.05060	0.05240
	tN_high_10_no	0.03036	0.04368	0.05060	0.05240
	tN_high_11_dR	0.02664	0.03830	0.04402	0.04580
	tN_high_12_LRJET_PT	0.02330	0.03596	0.04244	0.04444
	tN_high_13_LRJET_M	0.02082	0.03284	0.03910	0.04080
	tN_high_14_dphi	**0.01976**	**0.03062**	**0.03662**	**0.03844**

[1] G. Aad *et al.* (ATLAS Collaboration), Phys. Lett. B **716**, 1 (2012).
[2] S. Chatrchyan *et al.* (CMS Collaboration), Phys. Lett. B **716**, 30 (2012).
[3] Y. A. Golfand and E. P. Likhtman, JETP Lett. **13**, 323 (1971).
[4] P. Ramond, Phys. Rev. D **3**, 2415 (1971).
[5] A. Neveu and J. H. Schwarz, Phys. Rev. D **4**, 1109 (1971).
[6] D. V. Volkov and V. P. Akulov, Phys. Lett. B **46**, 109 (1973).
[7] S. Weinberg, Phys. Rev. D **13**, 974 (1976).
[8] L. Susskind, Phys. Rev. D **20**, 2619 (1979).
[9] A. Belyaev, M. S. Brown, R. Foadi, and M. T. Frandsen, Phys. Rev. D **90**, 035012 (2014).
[10] D. B. Kaplan, H. Georgi, and S. Dimopoulos, Phys. Lett. B **136**, 187 (1984).
[11] H. Georgi, D. B. Kaplan, and P. Galison, Phys. Lett. B **143**, 152 (1984).
[12] M. J. Dugan, H. Georgi, and D. B. Kaplan, Nucl. Phys. **B254**, 299 (1985).
[13] K. Agashe, R. Contino, and A. Pomarol, Nucl. Phys. **B719**, 165 (2005).
[14] It should be noted that CH models require UV completion with some new strong dynamics and therefore, TC and CH models can appear as different limits of strongly coupled theories [15].
[15] G. Cacciapaglia and F. Sannino, J. High Energy Phys. 04 (2014) 111.
[16] L. Randall and R. Sundrum, Phys. Rev. Lett. **83**, 3370 (1999).
[17] T. Gherghetta and A. Pomarol, Nucl. Phys. **B586**, 141 (2000).
[18] N. Arkani-Hamed, A. G. Cohen, E. Katz, A. E. Nelson, T. Gregoire, and J. G. Wacker, J. High Energy Phys. 08 (2002) 021.
[19] N. Arkani-Hamed, A. G. Cohen, E. Katz, and A. E. Nelson, J. High Energy Phys. 07 (2002) 034.
[20] M. Schmaltz and D. Tucker-Smith, Annu. Rev. Nucl. Part. Sci. **55**, 229 (2005).
[21] Z. Chacko, H.-S. Goh, and R. Harnik, Phys. Rev. Lett. **96**, 231802 (2006).
[22] N. Craig, S. Knapen, and P. Longhi, Phys. Rev. Lett. **114**, 061803 (2015).

[23] T. Han, R. Mahbubani, D. G. E. Walker, and L.-T. Wang, J. High Energy Phys. 05 (**2009**) 117.
[24] S. Kraml, U. Laa, L. Panizzi, and H. Prager, J. High Energy Phys. 11 (2016) 107.
[25] S. Baek, P. Ko, and P. Wu, J. High Energy Phys. 10 (2016) 117.
[26] D. Barducci and C. Delaunay, J. High Energy Phys. 02 (2016) 055.
[27] For earlier work on top partner models in the presence of colored vector resonances cf. e.g. [28].
[28] B. A. Dobrescu, K. Kong, and R. Mahbubani, J. High Energy Phys. 06 (2009) 001.
[29] The production of T'_d-pairs through QCD and Z' (with couplings $\lambda_{Z'T'_d\overline{T}'_d}$ instead of $\lambda_{Z'T'_s\overline{T}'_s}$) and their kinematical distributions of T'_d are basically identical to those of T'_s (see also the remark below about the small difference between various chirality combinations). One should note, though, that in case of T' doublet, the T'_d is accompanied by the charge $-\frac{1}{3}$ state B'_d, which by itself can be pair-produced through QCD or Z' and yields a $b\bar{b}+\not{E}_T$ signature, similar to the general $jj+\not{E}_T$ signature studied in the context of the QCD production of vectorlike quarks followed by their decay to light quarks and DM [30].
[30] F. Giacchino, A. Ibarra, L. L. Honorez, M. H. G. Tytgat, and S. Wild, J. Cosmol. Astropart. Phys. 02 (2016) 002.
[31] A. Semenov, Comput. Phys. Commun. **115**, 124 (1998).
[32] A. Semenov, Comput. Phys. Commun. **180**, 431 (2009).
[33] A. Semenov, arXiv:1005.1909.
[34] N. D. Christensen and C. Duhr, Comput. Phys. Commun. **180**, 1614 (2009).
[35] A. Alloul, N. D. Christensen, C. Degrande, C. Duhr, and B. Fuks, Comput. Phys. Commun. **185**, 2250 (2014).
[36] A. Belyaev, N. D. Christensen, and A. Pukhov, Comput. Phys. Commun. **184**, 1729 (2013).
[37] J. Alwall, R. Frederix, S. Frixione, V. Hirschi, F. Maltoni, O. Mattelaer, H.-S. Shao, T. Stelzer, P. Torrielli, and M. Zaro, J. High Energy Phys. 07 (**2014**) 079.
[38] M. Bondarenko *et al.*, arXiv:1203.1488.
[39] HEPMDB, http://hepmdb.soton.ac.uk/hepmdb:0717.0253.
[40] HEPMDB, http://hepmdb.soton.ac.uk/hepmdb:0717.0254.
[41] R. D. Ball, V. Bertone, S. Carrazza, L. Del Debbio, S. Forte, A. Guffanti, N. P. Hartland, and J. Rojo (NNPDF), Nucl. Phys. **B877**, 290 (2013).
[42] T. Sjostrand, S. Mrenna, and P. Z. Skands, Comput. Phys. Commun. **178**, 852 (2008).
[43] J. de Favereau, C. Delaere, P. Demin, A. Giammanco, V. Lemaître, A. Mertens, and M. Selvaggi (DELPHES 3 Collaboration), J. High Energy Phys. 02 (2014) 057.
[44] M. Cacciari and G. P. Salam, Phys. Lett. B **641**, 57 (2006).
[45] M. Cacciari, G. P. Salam, and G. Soyez, Eur. Phys. J. C **72**, 1896 (2012).
[46] M. Drees, H. Dreiner, D. Schmeier, J. Tattersall, and J. S. Kim, Comput. Phys. Commun. **187**, 227 (2015).
[47] D. Dercks, N. Desai, J. S. Kim, K. Rolbiecki, J. Tattersall, and T. Weber, Comput. Phys. Commun. **221**, 383 (2017).
[48] G. Aad *et al.* (ATLAS Collaboration), Eur. Phys. J. C **76**, 259 (2016).
[49] M. Aaboud *et al.* (ATLAS Collaboration), J. High Energy Phys. 06 (2016) 059.
[50] M. Aaboud *et al.* (ATLAS Collaboration), Phys. Rev. D **94**, 032005 (2016).
[51] M. Aaboud *et al.* (ATLAS Collaboration), Eur. Phys. J. C **76**, 392 (2016).
[52] G. Aad *et al.* (ATLAS Collaboration), Eur. Phys. J. C **76**, 565 (2016).
[53] G. Aad *et al.* (ATLAS Collaboration), Phys. Rev. D **94**, 032003 (2016).
[54] M. Aaboud *et al.* (ATLAS Collaboration), Phys. Rev. D **94**, 052009 (2016).
[55] (The ATLAS Collaboration), Technical Report No. ATLAS-CONF-2015-082, CERN, Geneva (2015).
[56] (The ATLAS Collaboration), Technical Report No. ATLAS-CONF-2016-013, CERN, Geneva (2016).
[57] (The ATLAS Collaboration), Technical Report No. ATLAS-CONF-2016-076, CERN, Geneva (2016), https://cds.cern.ch/record/2206249.
[58] (The ATLAS Collaboration), Technical Report No. ATLAS-CONF-2016-050, CERN, Geneva (2016).
[59] (CMS Collaboration), Technical Report No. CMS-PAS-SUS-15-011, CERN, Geneva (2015).
[60] G. Belanger, F. Boudjema, A. Pukhov, and A. Semenov, Comput. Phys. Commun. **185**, 960 (2014).
[61] G. Belanger, F. Boudjema, A. Pukhov, and A. Semenov, Comput. Phys. Commun. **176**, 367 (2007).
[62] G. Belanger, F. Boudjema, P. Brun, A. Pukhov, S. Rosier-Lees, P. Salati, and A. Semenov, Comput. Phys. Commun. **182**, 842 (2011).
[63] E. Aprile *et al.* (XENON Collaboration), Phys. Rev. Lett. **119**, 181301 (2017).
[64] HEPMDB, https://hepmdb.soton.ac.uk/phenodata/view.php?id=595e239abb817586383e929d.
[65] P. A. R. Ade *et al.* (Planck Collaboration), Astron. Astrophys. **571**, A16 (2014).
[66] P. Ade *et al.* (Planck Collaboration), Astron. Astrophys. **594**, A13 (2016).
[67] G. Aad *et al.* (ATLAS Collaboration), J. High Energy Phys. 01 (2016) 172.
[68] P. Athron *et al.* (GAMBIT Collaboration), Eur. Phys. J. C **77**, 568 (2017).
[69] To be precise, we plot the η distribution of the top quark added to the η distribution of the antitop.
[70] For simplicity, we do not consider finite width effects arising from the T'_s decays.
[71] S. Moretti, D. O'Brien, L. Panizzi, and H. Prager, Phys. Rev. D **96**, 035033 (2017).
[72] These searches focus mainly on SUSY-like final states with $\not{E}_T$ and are thus expected to yield relevant bounds on the $t\bar{t}\phi\phi$ (with ϕ representing $\not{E}_T$) final state which we investigate.
[73] (The ATLAS Collaboration), Technical Report No. ATLAS-CONF-2016-069, CERN, Geneva (2016).
[74] A. M. Sirunyan *et al.* (CMS Collaboration), arXiv:1611.03568.
[75] (The ATLAS Collaboration), Technical Report No. ATLAS-CONF-2016-045, CERN, Geneva (2016).
[76] (CMS Collaboration), Technical Report No. CMS-PAS-EXO-16-031, CERN, Geneva (2016).
[77] For illustration, Tables II and III give more details on four benchmark points included in Fig. 13.